



AFRL-RY-WP-TR-2011-1179

LEAKY WAVES IN METAMATERIALS FOR ANTENNA APPLICATIONS

Jiming Song

Iowa State University

JULY 2011

Final Report

Approved for public release; distribution unlimited.

See additional restrictions described on inside pages

STINFO COPY

**AIR FORCE RESEARCH LABORATORY
SENSORS DIRECTORATE
WRIGHT-PATTERSON AIR FORCE BASE, OH 45433-7320
AIR FORCE MATERIEL COMMAND
UNITED STATES AIR FORCE**

NOTICE AND SIGNATURE PAGE

Using Government drawings, specifications, or other data included in this document for any purpose other than Government procurement does not in any way obligate the U.S. Government. The fact that the Government formulated or supplied the drawings, specifications, or other data does not license the holder or any other person or corporation; or convey any rights or permission to manufacture, use, or sell any patented invention that may relate to them.

This report is the result of contracted fundamental research deemed exempt from public affairs security and policy review in accordance with SAF/AQR memorandum dated 10 Dec 08 and AFRL/CA policy clarification memorandum dated 16 Jan 09. This report is available to the general public, including foreign nationals. Copies may be obtained from the Defense Technical Information Center (DTIC) (<http://www.dtic.mil>).

AFRL-RY-WP-TR-2011-1179 HAS BEEN REVIEWED AND IS APPROVED FOR PUBLICATION IN ACCORDANCE WITH ASSIGNED DISTRIBUTION STATEMENT.

*//Signature//

DAVID D. CURTIS for ROBERT SHORE
Work Unit Manager
Antenna Technology Branch
Electromagnetics Technology Division

//Signature//

DAVID D. CURTIS
Branch Chief
Antenna Technology Branch
Electromagnetics Technology Division

//Signature//

WILLIAM E. MOORE, Division Chief
Electromagnetics Technology Division
Sensors Directorate

This report is published in the interest of scientific and technical information exchange, and its publication does not constitute the Government's approval or disapproval of its ideas or findings.

*Disseminated copies will show “//Signature//” stamped or typed above the signature blocks.

| REPORT DOCUMENTATION PAGE | | | | Form Approved OMB No. 0704-0188 | |
|--|-----------------------------|------------------------------|---------------------------------------|---|--|
| <p>The public reporting burden for this collection of information is estimated to average 1 hour per response, including the time for reviewing instructions, searching existing data sources, gathering and maintaining the data needed, and completing and reviewing the collection of information. Send comments regarding this burden estimate or any other aspect of this collection of information, including suggestions for reducing this burden, to Department of Defense, Washington Headquarters Services, Directorate for Information Operations and Reports (0704-0188), 1215 Jefferson Davis Highway, Suite 1204, Arlington, VA 22202-4302. Respondents should be aware that notwithstanding any other provision of law, no person shall be subject to any penalty for failing to comply with a collection of information if it does not display a currently valid OMB control number. PLEASE DO NOT RETURN YOUR FORM TO THE ABOVE ADDRESS.</p> | | | | | |
| 1. REPORT DATE (DD-MM-YY) July 2011 | | 2. REPORT TYPE Final | | 3. DATES COVERED (From - To) 14 January 2010 – 18 April 2011 | |
| 4. TITLE AND SUBTITLE LEAKY WAVES IN METAMATERIALS FOR ANTENNA APPLICATIONS | | | | 5a. CONTRACT NUMBER FA8718-10-C-0006 | |
| | | | | 5b. GRANT NUMBER | |
| | | | | 5c. PROGRAM ELEMENT NUMBER 62204F | |
| 6. AUTHOR(S) Jiming Song | | | | 5d. PROJECT NUMBER 4916 | |
| | | | | 5e. TASK NUMBER HA | |
| | | | | 5f. WORK UNIT NUMBER 4916HACQ | |
| 7. PERFORMING ORGANIZATION NAME(S) AND ADDRESS(ES) Iowa State University 1350 Beardshear Hall Ames, IA 50011-2025 | | | | 8. PERFORMING ORGANIZATION REPORT NUMBER | |
| 9. SPONSORING/MONITORING AGENCY NAME(S) AND ADDRESS(ES) Air Force Research Laboratory Sensors Directorate Wright-Patterson Air Force Base, OH 45433-7320 Air Force Materiel Command United States Air Force | | | | 10. SPONSORING/MONITORING AGENCY ACRONYM(S) AFRL/RHYA | |
| | | | | 11. SPONSORING/MONITORING AGENCY REPORT NUMBER(S) AFRL-RY-WP-TR-2011-1179 | |
| 12. DISTRIBUTION/AVAILABILITY STATEMENT Approved for public release; distribution unlimited. | | | | | |
| 13. SUPPLEMENTARY NOTES This report is the result of fundamental research authored by university. As such, the material does not require Public Affairs (PA) Office security and policy review prior to releasing the information to the public. This report contains color. | | | | | |
| 14. ABSTRACT Focus was on investigating leaky waves and their excitation with multilayered metamaterials to enhance antenna performance: wave propagation along a grounded dielectric slab with double negative (DNG) materials, complex waves (leaky waves) changes with different material parameters, electric size (frequency and thickness) and loss, Sommerfeld integral path for evaluating fields accurately and efficiently, the radiation intensity and directivity of electric/magnetic dipoles over a grounded slab, and optimization of the directivity over the thickness and the constitutive parameters for antenna applications of interest to the Air Force. | | | | | |
| 15. SUBJECT TERMS leaky waves, double negative (DNG) metamaterials, grounded slab, Sommerfeld integral path, optimized directivity, antennas | | | | | |
| 16. SECURITY CLASSIFICATION OF: | | | 17. LIMITATION OF ABSTRACT: SAR | 18. NUMBER OF PAGES 68 | 19a. NAME OF RESPONSIBLE PERSON (Monitor) David D. Curtis 19b. TELEPHONE NUMBER (Include Area Code) N/A |
| a. REPORT Unclassified | b. ABSTRACT Unclassified | c. THIS PAGE Unclassified | | | |

Contents

| | | |
|----------|--|-----------|
| 1 | Executive Summary | 1 |
| 2 | Introduction | 3 |
| 3 | Mode Properties and Surface Pole Loci | 5 |
| 3.1 | Eigen Value Problem | 5 |
| 3.1.1 | Decoupling of TE and TM Modes | 5 |
| 3.1.2 | Homogeneous Helmholtz Equation | 6 |
| 3.1.3 | Boundary Conditions | 7 |
| 3.1.4 | Discrete TE Modes | 7 |
| 3.1.5 | Discrete TM Modes | 8 |
| 3.1.6 | Field Components of Discrete TE and TM Modes | 9 |
| 3.1.7 | Graphical Method | 9 |
| 3.2 | Mode Properties | 12 |
| 3.2.1 | Evanescent Surface Wave Modes | 12 |
| 3.2.2 | Complex Surface Modes and Its Poynting Vectors | 13 |
| 3.3 | Mode Spectrum of DNG Medium | 17 |
| 3.4 | Dispersion Diagrams and Power Flow | 20 |
| 3.5 | The Leaky Modes | 22 |
| 3.6 | Mode Loci vs. Frequency/Thickness | 23 |
| 3.7 | Mode Loci vs. Loss | 27 |
| 4 | Sommerfeld Integral Path and Numerical Considerations | 29 |
| 4.1 | Spectral Domain Approach | 29 |
| 4.1.1 | Hertz Potentials | 29 |
| 4.1.2 | Fourier Transforms | 30 |
| 4.1.3 | TE Fields in Cylindrical Coordinate | 31 |
| 4.1.4 | TM Fields in Cylindrical Coordinate | 32 |
| 4.1.5 | Rewriting as Infinite Integrals | 32 |
| 4.1.6 | Total Fields in Cylindrical Coordinate | 33 |
| 4.1.7 | Solving \tilde{F}_e and \tilde{F}_h | 35 |
| 4.2 | Sommerfeld Integral Path (SIP) | 37 |
| 4.3 | Residue at Origin | 40 |
| 4.4 | Numerical Integration Along SIP | 43 |

5 Numerical Examples and Optimization for Directivity 45

5.1 Numerical Example of New SIP Path for DNG Media 45

5.2 The Discrete Pole Contribution of DNG Media 46

5.3 3-D Radiation Patterns (linear scale) of HED and HMD with DNG Media 48

5.4 Optimization for Directivity 48

6 Conclusions, Publications, and Significant Events 53

Abstract We report the main results produced within the effort sponsored by the U.S. Air Force Research Laboratory with Contract No. FA8718-09-C-0006. We focus on investigating leaky waves and their excitation with multilayered metamaterials to enhance antenna performance: wave propagation along a grounded dielectric slab with double negative (DNG) materials, complex waves (leaky waves) changes as different material parameters, electric size (frequency and thickness) and loss, Sommerfeld integral path for evaluating fields accurately and efficiently, the radiation intensity and directivity of electric/magnetic dipoles over a grounded slab, and optimization of the directivity over the thickness and the constitutive parameters for antenna applications of interest to the Air Force.

Acknowledgments We are very thankful to the relevant and fruitful interactions with Dr. Robert A. Shore and Dr. Arthur D. Yaghjian on several problems tackled and solved in this project and comments and suggestions on this report.

1 Executive Summary

Metamaterials such as left-handed materials (LHMs), where both permittivity and permeability are negative, have attracted great attention due to their novel and unique electromagnetic properties. The metamaterials have potential applications such as radio frequency and microwave device miniaturization. Because excited complex surface modes have slowly exponential decaying fields on the air-slab interface, the directivity for dipoles over a grounded metamaterial slab is much higher than directivity with conventional double positive (DPS) materials. This structure is very useful to study slot antennas and leaky-wave antennas.

We propose to investigate leaky waves and their excitation with multilayered metamaterials. The objective of this project is to enhance antenna performance with excitations of leaky waves. First, we investigate a grounded dielectric slab with double negative (DNG) materials. Dramatically different dispersion curves of evanescent surface modes (electromagnetic fields that exponentially decay both in air and inside the slab) are observed, indicating that they are highly dependent on the medium parameters. As the counterpart of the improper complex leaky modes in a slab with a double positive (DPS) medium, the complex modes in a slab with a DNG medium are proven to be exclusively proper. They have exponentially decaying fields in the air region and are termed complex surface modes. There are an infinite number of complex surface modes and they cannot be suppressed. Further investigation of the Poynting vector shows that those complex modes do not carry away power in both transverse and longitudinal directions. However, the complex surface modes play an important role in the far field radiating from the interface between the air region and the grounded slab.

Secondly, we read Tamir and Kou's paper and other papers on leaky waves in asymmetric slabs. By 'Asymmetric' it means that the material above and below the slab can have different dielectric constant, which makes the discussion more general. Tamir and Kou claim that there are eight different leaky-wave fields guided by an asymmetric layer configuration, but only four of the eight can be excited in conventional DPS materials. Those eight leaky waves can be divided into four forward and four backward leaky waves, or four co- and four contra-leaky waves. It is found that for a lossless DPS grounded slab, there are only two improper complex modes (leaky waves). If the slab is lossy, the conventional surface wave modes become complex modes, which are called leaky waves by Tamir and Kou. A plasma slab will add another type of proper complex modes. For a grounded slab with DNG materials, only two proper regular complex modes exist for a lossless slab. If the slab is lossy, the proper surface wave modes may become proper complex modes or improper complex modes.

Thirdly, we investigated the Sommerfeld integral path (SIP) for dielectric slab with double

negative metamaterials. It is found that layered double negative materials have different SIPs as compared to conventional layered double positive media. In a layered medium, the Green's function is written as a Sommerfeld-type integral, whose integrand has poles on the k_ρ -plane which correspond to the eigenmode solutions of the same structure with the source removed. After the proper integral path has been established, there are two ways to represent the total field. The first one is often to deform the path to a branch cut (BC) with poles captured by the branch cut, which leads to a spectral representation. The second way is to deform the path to a steepest descent path (SDP) with poles captured, which lead to a non-spectral representation for calculating far field (from the integral along the SDP directly). When the medium is lossless, the Sommerfeld integral blows up at real surface poles along the real axis. A common way to address this difficulty is to assume that the medium is lossy and then monitor how pole loci change as the loss becomes smaller and smaller. From our previous results, the Sommerfeld integral path is chosen as a half circle above or below the poles depending on the kind of poles, the first kind or second kind. Physically the first kind of poles corresponds to forward surface modes (the power flow is in the same direction as the wave propagation), while the second kind of poles corresponds to backward surface modes (the power flow is in the opposite direction as the wave propagation). We'll talk about the poles in details in Section 3.

Finally, we investigated the radiation intensity and directivity of electric/magnetic dipoles over a grounded slab to find optimal values of material parameters and thickness for a given frequency. We considered a horizontal magnetic dipole (HMD) placed on a PEC and covered by a layer of DNG material with thickness d and constitutive parameters ϵ_r and μ_r . The material is homogeneous, isotropic, non-dispersive. We optimize the directivity over the thickness and the constitutive parameters. It is found that for a slab with a fixed electric size (proportional to the product of the thickness and frequency), the directivity reaches the maximum when the product of ϵ_r and μ_r is a certain value, which is determined by the electric size only. The maximum directivity is proportional to ϵ_r and $(d/\lambda_0)^{8/3}$. We also found the fitting formula for the maximum directivity and μ_r as functions of the electric size and ϵ_r .

This final project report is organized as follows: The second section gives a brief introduction to this field. Section 3 briefly reviews the mode properties, dispersion diagrams, and power flows and plots pole loci versus frequency and media loss. Section 4 discusses the proposed new Sommerfeld integral path and addresses two numerical issues associated with Sommerfeld integral that are generally overlooked by the literature. Section 5 gives several numerical examples that demonstrate the necessity of the new SIP for DNG media, and the superior radiation patterns of a simple dipole antenna filled with DNG media. We also optimize structure for maximum directivity of HMD at the broadside. Finally, Section 6 concludes the report with a summary, publication list, significant events, and proposed future work.

2 Introduction

Due to the progress in fabrication technology and nanotechnology, there is a renewed interest in developing composite materials that mimic known material responses or that qualitatively have new, physically realizable response functions that do not occur in nature [1]. Examples of engineered materials include left-hand materials (LHMs), negative refraction materials, electromagnetic band-gap (EBG) structured materials, and complex impedance surfaces. Those new metamaterials often are generated by artificially fabricated inhomogeneities embedded in host media.

The metamaterials have potential applications such as radio frequency and microwave device miniaturization. Microstrip antennas are easy to make and have the advantages of small size, light weight, and low cost. Surface waves always exist on grounded conventional dielectric slabs, carry away energy, and reduce antenna directivity. Leaky waves are a type of complex surface waves and have slowly exponential decaying fields along the air-slab interface. The leaky waves make the fields on the interface equivalent to an antenna with large aperture, which leads to the directivity for dipoles over a grounded metamaterial slab is much higher than directivity with conventional double positive (DPS) materials. This structure is very useful to study slot antennas and leaky-wave antennas.

Pendry et al. proposed forming LHMs by introducing a periodic array of split ring resonators and continuous wires [2]. LHMs have been demonstrated experimentally by Smith et al. and Shelby et al. [3, 4]. Double negative (DNG) metamaterials have attracted intensive interest in the last few years for their exotic properties, such as negative refraction, reversed Doppler effect, reversed Vavilov-Cerenkov effect, and the possibility of making perfect lens [5, 6, 2, 7, 3, 8, 9, 10, 11, 12, 13, 14, 15]. Many researchers have shown great interest in antenna applications of metamaterials [1, 16, 17, 18, 19, 20]. Ziolkowski and Kipple [16] showed analytically that the LHMs increase radiation efficiency of small simple antennas. An electric or magnetic dipole radiating in a grounded dielectric slab with ideal LHMs has been studied numerically and the proper complex modes (leaky waves) result in a radiation pattern like a pencil beam at broadside [21, 22].

Among the many applications and novel structures proposed for double negative metamaterials, the grounded dielectric slab with a DNG medium is the most fundamental structure because it not only is the theoretical foundations for other more complicated structures but also has many potential applications such as transmission line in real systems. [23] and [24] found that there are special regions for transverse magnetic (TM) modes where two different propagation constants exist. [25, 17, 26, 27] studied evanescent surface modes, which do not exist in a double positive (DPS) medium. The grounded dielectric slab also supports complex surface modes even for lossless media [28, 18, 27]. Baccarelli and his colleagues proposed the concept of surface wave suppression,

which ensures the absence of both ordinary and evanescent surface modes. This is very attractive in view of taking the DNG medium as a potential substrate candidate to reduce edge diffraction effects and enhance radiation efficiency for microstrip antennas [29, 21]. Later, the necessary and sufficient conditions for surface wave suppressions were derived in [30, 27].

In [18], radiations from a magnetic dipole on grounded dielectric slab with DNG medium are studied. In analyzing such problems, the spectral domain approach is used and consists of two steps: first, the electromagnetic fields generated by a dipole are solved in the spectral domain via a Fourier transform; the spectral domain solution is then transformed back to the space domain. The second step involves a Sommerfeld-type integral (integral from zero to infinity). For a lossless medium there are a branch-cut issue and surface mode singularity blow-up problem [31]. A common way to remedy the aforementioned difficulties is to firstly assume that dielectric medium is lossy and then let the loss decrease to zero [32]. With this method, the Sommerfeld integral path (SIP) for conventional lossless medium is well-defined [31].

However, the grounded dielectric slab with a DNG medium has a mode spectrum that is much more complicated than that of a conventional double positive medium [27]. Its complete eigenmode spectrum consists of evanescent surface modes, ordinary surface modes, complex surface modes, and continuous radiation modes. By contrast, the complete mode spectrum of a DPS medium consists of only ordinary surface modes and radiation modes. In addition to the mode expansion, the ordinary surface modes of a DNG medium bifurcate near their cutoff frequencies. Both of these two phenomena contribute to the novel properties of the DNG medium. On the other hand, they make the problems related to DNG medium more complicated. One of the most significant ramifications is that a DNG medium requires a different Sommerfeld integral path, which will be elaborated on in this report in great detail.

3 Mode Properties and Surface Pole Loci

3.1 Eigen Value Problem

The structure we investigate is a grounded dielectric slab of thickness d (see Figure 1). Region I is air with ϵ_{r1} and μ_{r1} and Region II is a DNG medium ϵ_{r2} and μ_{r2} . Inherently, the passive DNG media must be dispersive [9,33]. However, as is common in the literature, most of the DNG medium considered in this paper is assumed to be non-dispersive for simplicity purpose. This assumption is found acceptable because a small perturbation of ϵ_r and μ_r satisfies its dispersiveness.

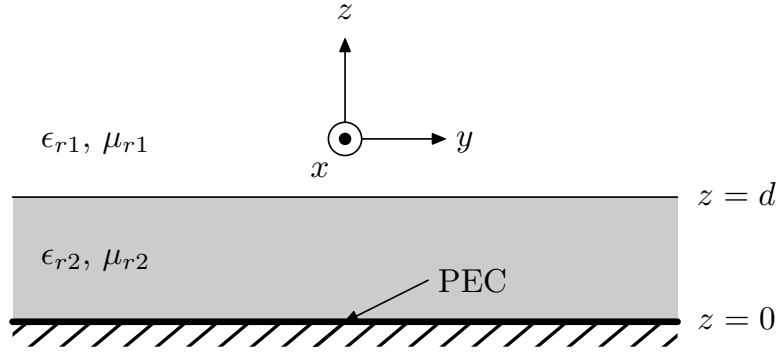


Figure 1: A grounded dielectric slab with lossless, isotropic and homogeneous DNG medium.

3.1.1 Decoupling of TE and TM Modes

For homogeneous isotropic medium, the two curl equations in source free region

$$\nabla \times \mathbf{E} = -j\omega\mu\mathbf{H} \quad (1)$$

$$\nabla \times \mathbf{H} = j\omega\epsilon\mathbf{E} \quad (2)$$

are expanded into six scalar equations

$$\frac{\partial E_y}{\partial z} + \gamma_y E_z = j\omega\mu H_x \quad (3a)$$

$$-\gamma_y E_x = j\omega\mu H_z \quad (3b)$$

$$-\frac{\partial E_x}{\partial z} = j\omega\mu H_y \quad (3c)$$

$$\frac{\partial H_y}{\partial z} + \gamma_y H_z = -j\omega\epsilon E_x \quad (3d)$$

$$\gamma_y H_x = j\omega\epsilon E_z \quad (3e)$$

$$\frac{\partial H_x}{\partial z} = j\omega\epsilon E_y \quad (3f)$$

In deriving the above equations, $\partial/\partial x = 0$ and $\partial/\partial y = -\gamma_y$ are used.

Equations (3a), (3e), and (3f) are functions of E_y , E_z , and H_x only. And (3b), (3c), and (3d) are functions of H_y , H_z , and E_x only. This observation implies that under the condition of $\partial/\partial x = 0$, the electromagnetic waves are decoupled into independent TE modes (H_y , H_z , E_x) and TM modes (E_y , E_z , H_x). Notice that in this chapter, TE and TM modes are referred to horizontal propagation direction (y -direction in Figure 1). This classification is also applicable to vertical direction (z -direction in Figure 1) as will be seen in later chapters.

3.1.2 Homogeneous Helmholtz Equation

Substituting (3b) and (3c) into (3d), we arrive at 1-D homogeneous Helmholtz equation for TE modes propagating along y -direction

$$\frac{d^2 E_x}{dz^2} + (k_i^2 + \gamma_y^2) E_x = 0 \quad (4)$$

where $k_i^2 = \omega^2 \epsilon_i \mu_i$, $i = 1, 2$, and

$$\gamma_y = \alpha + j\beta \quad (5)$$

With the same procedure, we have 1-D homogeneous Helmholtz equation for TM modes

$$\frac{d^2 H_x}{dz^2} + (k_i^2 + \gamma_y^2) H_x = 0 \quad (6)$$

3.1.3 Boundary Conditions

Equations (4) and (6) are 1-D differential equations valid for each source free region. Boundary conditions must be applied to solve the problem.

At the interface of Region 1 and Region 2, tangential electric and magnetic fields are continuous. So for TE modes

$$E_{x1} \big|_{z=d} = E_{x2} \big|_{z=d} \quad (7a)$$

$$H_{y1} \big|_{z=d} = H_{y2} \big|_{z=d} \quad (7b)$$

For TM modes

$$E_{y1} \big|_{z=d} = E_{y2} \big|_{z=d} \quad (8a)$$

$$H_{x1} \big|_{z=d} = H_{x2} \big|_{z=d} \quad (8b)$$

In Region 1, proper boundary condition requires vanishing field at infinity

$$\Lambda \big|_{z=\infty} = 0 \quad (9)$$

or radiation condition [34]

$$\lim_{r \rightarrow \infty} r \left[\frac{\partial \Lambda}{\partial r} + jk\Lambda \right] = 0 \quad (10)$$

where $\Lambda = E_{x1}$ for TE modes and $\Lambda = H_{x1}$ for TM modes. Notice that (9) is a special case of (10). Solutions do not satisfy (10) are non-physical. However, they are still of importance as we will see later.

In Region 2, there is boundary conditions of PEC at $z = 0$. For TE modes

$$E_{x2} \big|_{z=0} = 0 \quad (11)$$

For TM modes

$$\frac{\partial H_{x2}}{\partial z} \bigg|_{z=0} = 0 \quad (12)$$

3.1.4 Discrete TE Modes

The general solutions of (4) in region 1 and region 2 are

$$E_{x1} = Ae^{-\gamma_{z1}(z-d)} + Be^{\gamma_{z1}(z-d)} \quad (13)$$

$$E_{x2} = Ce^{-\gamma_{z2}z} + De^{\gamma_{z2}z} \quad (14)$$

where $\gamma_{zi}^2 = -k_0^2 \epsilon_{ri} \mu_{ri} - \gamma_y^2$ and $i = 1, 2$ is the layer index.

To satisfy boundary condition of (11), we have $C = -D$ or

$$E_{x2} = C \sinh(\gamma_{z2} z) \quad (15)$$

Surface waves have zero field at infinity. Thus in (13), one term must be removed. The choice is arbitrary since we have two different choices for γ_{z1} too. For example, one can choose $E_{x1} = B e^{\gamma_{z1}(z-d)}$ and $\gamma_{z1} = -\sqrt{-k_0^2 \epsilon_{r1} \mu_{r1} - \gamma_y^2}$. This is the same as the choice of $E_{x1} = A e^{-\gamma_{z1}(z-d)}$ and $\gamma_{z1} = \sqrt{-k_0^2 \epsilon_{r1} \mu_{r1} - \gamma_y^2}$. To be consistent with literature, we use $E_{x1} = A e^{-\gamma_{z1}(z-d)}$ and assume γ_{z1} has positive real part.

With the above observation, E_x and H_y in each region are

$$E_{x1} = A e^{-\gamma_{z1}(z-d)} \quad (16a)$$

$$E_{x2} = C \sinh(\gamma_{z2} z) \quad (16b)$$

$$H_{y1} = -\frac{1}{j\omega\mu_1} \frac{\partial E_{x1}}{\partial z} = \frac{\gamma_{z1}}{j\omega\mu_1} A e^{-\gamma_{z1}(z-d)} \quad (16c)$$

$$H_{y2} = -\frac{1}{j\omega\mu_2} \frac{\partial E_{x2}}{\partial z} = -\frac{\gamma_{z2}}{j\omega\mu_2} C \cosh(\gamma_{z2} z) \quad (16d)$$

Using boundary condition of (7), we have

$$\begin{bmatrix} 1 & -\sinh(\gamma_{z2} d) \\ \frac{\gamma_{z1}}{\mu_{r1}} & \frac{\gamma_{z2}}{\mu_{r2}} \cosh(\gamma_{z2} d) \end{bmatrix} \begin{bmatrix} A \\ C \end{bmatrix} = 0$$

Non-trivial solutions require the determinant of the matrix to be zero. Therefore we arrive at eigen equation for TE modes

$$\frac{\gamma_{z1}}{\mu_{r1}} \sinh(\gamma_{z2} d) + \frac{\gamma_{z2}}{\mu_{r2}} \cosh(\gamma_{z2} d) = 0 \quad (17)$$

where $\gamma_{z2} \neq 0$. To implicitly eliminate the fake solution of $\gamma_{z2} = 0$, (17) is written as

$$\frac{\mu_{r2}}{\gamma_{z2}} \sinh(\gamma_{z2} d) + \frac{\mu_{r1}}{\gamma_{z1}} \cosh(\gamma_{z2} d) = 0 \quad (18)$$

3.1.5 Discrete TM Modes

With the same procedure, eigen equation for TM modes is

$$\frac{\gamma_{z2}}{\epsilon_{r2}} \sinh(\gamma_{z2} d) + \frac{\gamma_{r1}}{\epsilon_{z1}} \cosh(\gamma_{z2} d) = 0 \quad (19)$$

3.1.6 Field Components of Discrete TE and TM Modes

The field components of discrete TE modes are ($\gamma_{z2} \neq 0$)

$$E_{x1}(y, z) = -\sinh(\gamma_{z2}d)e^{-\gamma_{z1}(z-d)}e^{-\gamma_y y} \quad (20a)$$

$$E_{x2}(y, z) = -\sinh(\gamma_{z2}z)e^{-\gamma_y y} \quad (20b)$$

$$H_{y1}(y, z) = -\frac{1}{j\omega\mu_1} \frac{\partial E_{x1}}{\partial z} = -\frac{\gamma_{z1}}{j\omega\mu_1} \sinh(\gamma_{z2}d)e^{-\gamma_{z1}(z-d)}e^{-\gamma_y y} \quad (20c)$$

$$H_{y2}(y, z) = -\frac{1}{j\omega\mu_2} \frac{\partial E_{x2}}{\partial z} = \frac{\gamma_{z2}}{j\omega\mu_2} \cosh(\gamma_{z2}z)e^{-\gamma_y y} \quad (20d)$$

$$H_{z1}(y, z) = -\frac{\gamma_y}{j\omega\mu_1} E_{x1} = \frac{\gamma_y}{j\omega\mu_1} \sinh(\gamma_{z2}d)e^{-\gamma_{z1}(z-d)}e^{-\gamma_y y} \quad (20e)$$

$$H_{z2}(y, z) = -\frac{\gamma_y}{j\omega\mu_2} E_{x2} = \frac{\gamma_y}{j\omega\mu_2} \sinh(\gamma_{z2}z)e^{-\gamma_y y} \quad (20f)$$

The field components of discrete TM modes are

$$H_{x1}(y, z) = -\cosh(\gamma_{z2}d)e^{-\gamma_{z1}(z-d)}e^{-\gamma_y y} \quad (21a)$$

$$H_{x2}(y, z) = -\cosh(\gamma_{z2}z)e^{-\gamma_y y} \quad (21b)$$

$$E_{y1}(y, z) = \frac{1}{j\omega\epsilon_1} \frac{\partial H_{x1}}{\partial z} = \frac{\gamma_{z1}}{j\omega\epsilon_1} \cosh(\gamma_{z2}d)e^{-\gamma_{z1}(z-d)}e^{-\gamma_y y} \quad (21c)$$

$$E_{y2}(y, z) = \frac{1}{j\omega\epsilon_2} \frac{\partial H_{x2}}{\partial z} = -\frac{\gamma_{z2}}{j\omega\epsilon_2} \sinh(\gamma_{z2}z)e^{-\gamma_y y} \quad (21d)$$

$$E_{z1}(y, z) = \frac{\gamma_y}{j\omega\epsilon_1} E_{x1} = -\frac{\gamma_y}{j\omega\epsilon_1} \cosh(\gamma_{z2}d)e^{-\gamma_{z1}(z-d)}e^{-\gamma_y y} \quad (21e)$$

$$E_{z2}(y, z) = \frac{\gamma_y}{j\omega\epsilon_2} E_{x2} = -\frac{\gamma_y}{j\omega\epsilon_2} \cosh(\gamma_{z2}z)e^{-\gamma_y y} \quad (21f)$$

3.1.7 Graphical Method

For ordinary real surface modes, $\gamma_{z1} = \alpha_{z1}$ and $\gamma_{z2} = j\beta_{z2}$, where both α_{z1} and β_{z2} are real numbers. Therefore (18) and (19) are rewritten as follows

$$\frac{\mu_{r1}}{\mu_{r2}}(\beta_{z2}d) \cot(\beta_{z2}d) = -\alpha_{z1}d \quad \text{for TE mode} \quad (22)$$

$$\frac{\epsilon_{r1}}{\epsilon_{r2}}(\beta_{z2}d) \tan(\beta_{z2}d) = \alpha_{z1}d \quad \text{for TM mode} \quad (23)$$

Furthermore, using relations $\gamma_{zi}^2 = -k_0^2\epsilon_{ri}\mu_{ri} - \gamma_y^2$ and $i = 1, 2$ and eliminating γ_y lead to

$$(\alpha_{z1}d)^2 + (\beta_{z2}d)^2 = (k_0d)^2(\epsilon_{r2}\mu_{r2} - \epsilon_{r1}\mu_{r1}) \quad (24)$$

The evanescent surface modes have exponentially decaying electromagnetic fields in both air and dielectric layer. For evanescent surface modes, $\gamma_{z1} = \alpha_{z1}$ and $\gamma_{z2} = \alpha_{z2}$, where both α_{z1} and α_{z2} are real numbers. The eigen equations (18) and (19) are rewritten as

$$\frac{\mu_{r1}}{\mu_{r2}}(\alpha_{z2}d) \coth(\alpha_{z2}d) = -\alpha_{z1}d \quad \text{for TE mode} \quad (25)$$

$$\frac{\epsilon_{r1}}{\epsilon_{r2}}(\alpha_{z2}d) \tanh(\alpha_{z2}d) = -\alpha_{z1}d \quad \text{for TM mode} \quad (26)$$

The constitutive equations are now

$$(\alpha_{z1}d)^2 - (\alpha_{z2}d)^2 = (k_0d)^2(\epsilon_{r2}\mu_{r2} - \epsilon_{r1}\mu_{r1}) \quad (27)$$

The graphical representations [35, 36] of the above equations are shown in Figure 2. In fact the figure combines two figures. The right-half is for the ordinary modes governed by Equations (22) to (24), and the left half is for the evanescent modes governed by Equations (25) to (27). The index notation used here follows [35]: only TE even modes (but with odd indices, $\text{TE}_1, \text{TE}_3, \dots$) and TM odd modes (but with even indices, $\text{TM}_0, \text{TM}_2, \dots$) can exist in a PEC grounded dielectric slab. Notice that in the first and second quadrants, α_{z1} is positive and the fields exponentially decay in the air region (proper); in the third and fourth quadrants, α_{z1} is negative and the fields exponentially increase in the air region (improper). The x -axis is divided into two segments. The right half is for $\beta_{z2}d$, whose fields inside the dielectric layer are sine/cosine standing waves (ordinary); while the left half is for $\alpha_{z2}d$, whose fields inside the dielectric layer are exponentially distributed (evanescent). The intersection in the second quadrant represents the proper evanescent surface mode which does not exist for a DPS medium. This can be seen from (22), (23), (25), and (26): the difference for DPS and DNG media is a minus sign on the left sides of these equations, which implies that one can get results for a DPS medium by mirroring Figure 2 along its horizontal axis. By doing this, the intersection in the second quadrant will be in the third quadrant, and thus improper.

Another important fact that must be recognized from Figure 2 is that the ordinary surface wave solutions for a DNG medium are no longer monotonic. It is clear from the sub-figure in the left corner of Figure 2(a) that there are two intersections as the radius of the dashed circle decreases, which corresponds to a decrease in electric size, *i.e.*, k_0d . Once the circle has only one tangential point with the solid line, further decreasing k_0d will cause this mode to be cutoff. Similar occurrence happens to TM modes in Figure 2(b) in a more obvious way. These two possible modes have two different power distributions. One has more power flowing in the air region than that in the dielectric region, making the total power flow in the same direction as the phase velocity. The other is in the opposite way and displays the backward property. More details on the Poynting vectors are addressed in later sections.

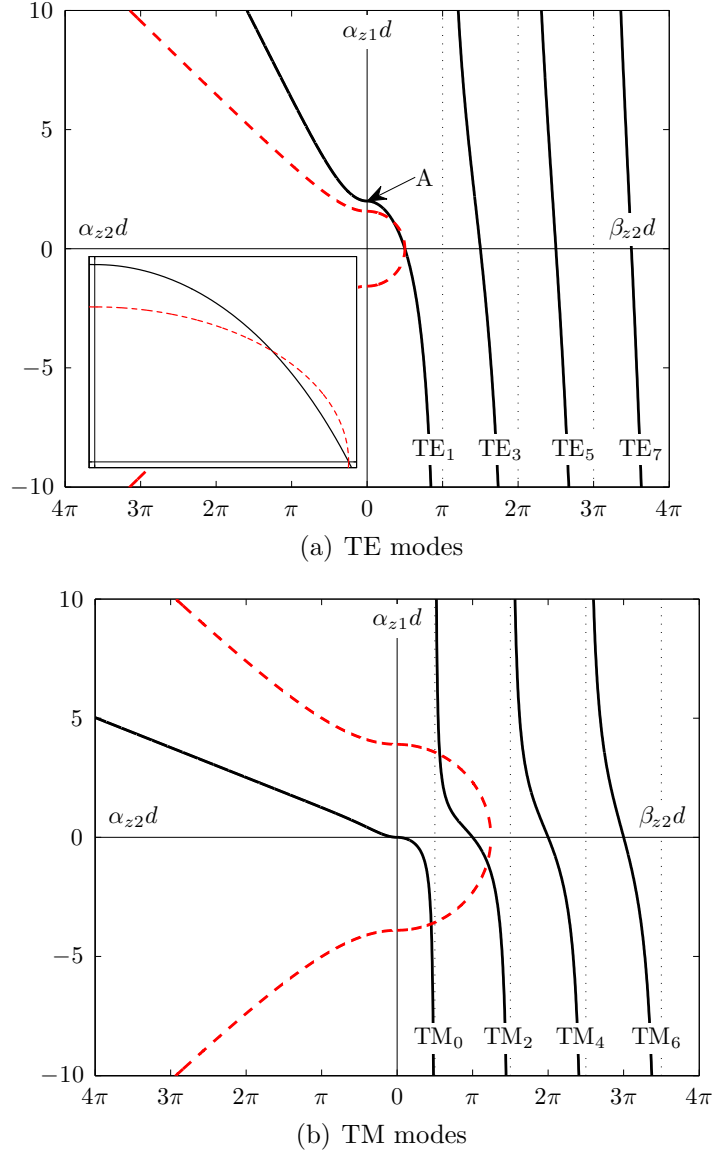


Figure 2: Graphical solutions for TE and TM modes. Solid lines in the first and fourth quadrants represent (22) or (23); solid lines in the second quadrant represent (25) or (26); dashed line in the first and fourth quadrants represents (24); dashed line in the second and third quadrants represents (27). The medium parameters are: $\epsilon_{r1} = 1$, $\mu_{r1} = 1$, $\epsilon_{r2} = -2.5$, $\mu_{r2} = -0.5$.

3.2 Mode Properties

This section states different mode properties, such as evanescent surface modes, complex surface modes, Poynting vectors, *etc.* We define some terms here first.

Discrete or continuous modes: Discrete modes refer to discrete solutions of eigen equations derived in last section and continuous modes are the waves satisfying the radiation boundary condition and having continuous spectrum, which are the contribution for the integral along the branch cuts.

Proper or improper modes: Proper modes exist physically and the fields of the improper modes increase exponentially to infinity at the infinity. So the improper modes cannot exist physically and are not part of complete spectrum. For the improper modes, $\alpha_{z1} = \text{Re}[\gamma_{z1}] < 0$. For the proper modes, $\text{Re}[\gamma_{z1}] \geq 0$. The modes with $\text{Re}[\gamma_{z1}] > 0$ are also called surface wave modes because the fields decay exponentially away from the interface in the top region.

Real or complex modes: For a lossless slab, the waves with a real propagation constant (γ_y or γ_ρ) are called as real modes, otherwise, they are called as complex modes. In general, all modes are complex for a lossy slab.

Ordinary or evanescent modes: Two types of real modes may be supported by a lossless slab: ordinary modes (standing waves in the dielectric region, $\alpha_{z2} = \text{Re}[\gamma_{z2}] = 0$) and evanescent modes (the fields change exponentially in the dielectric region, $\beta_{z2} = \text{Im}[\gamma_{z2}] = 0$).

3.2.1 Evanescent Surface Wave Modes

The normalized effective dielectric constant $\epsilon_{eff} = (\beta/k_0)^2$ for evanescent surface wave modes is larger than both $\epsilon_{r1}\mu_{r1}$ and $\epsilon_{r2}\mu_{r2}$. Therefore $\gamma_{z2} = \sqrt{-k_0^2\epsilon_{r2}\mu_{r2} - \gamma_y^2} = k_0\sqrt{\epsilon_{eff} - \epsilon_{r2}\mu_{r2}}$ is a pure real number. The electromagnetic fields inside the dielectric layer are no longer sine/cosine standing waves, but of the form of $A \sinh(\alpha_{z2}d)$. Figure 3 shows a typical field configuration for evanescent surface wave modes. Notice that the field extends to the air region far away and decay very slowly.

It is found that the dispersion curves for evanescent surface wave modes are complicated and highly dependent on medium parameters. Figure 4 shows two dispersion diagrams for TE₁ mode with different medium parameters. The solid line in Figure 4 is for proper mode while the dotted line is for improper mode. The dashed lines in both figures depict the value of $\sqrt{\epsilon_{r2}\mu_{r2}}$. They are the watersheds by which one can tell evanescent surface wave modes from ordinary ones.

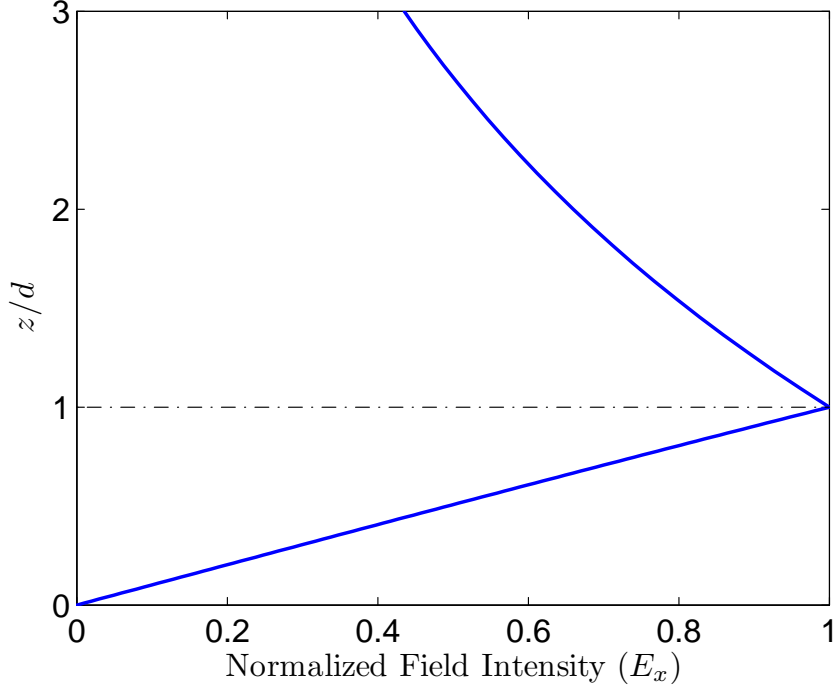
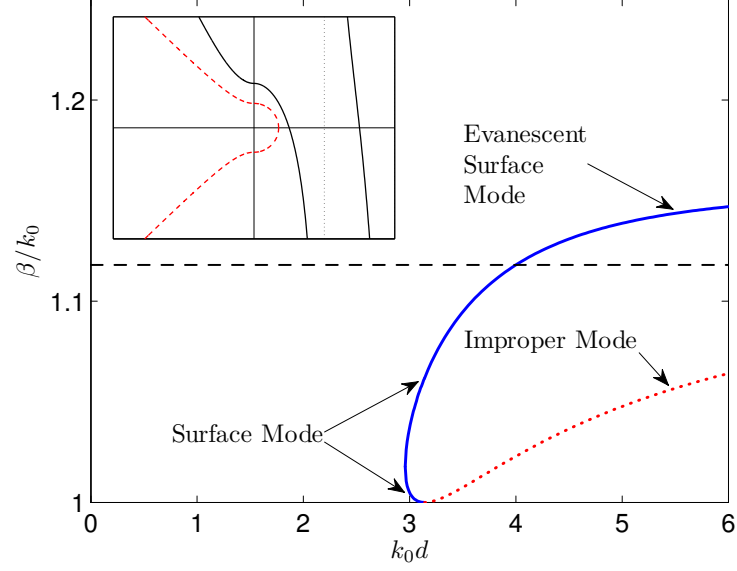


Figure 3: Demonstration of field distribution for a TE evanescent surface wave mode. Medium and structure parameters are: $\epsilon_{r1} = 1$, $\mu_{r1} = 1$, $\epsilon_{r2} = -2.5$, $\mu_{r2} = -2.5$, $k_0d = 0.1$ rad. Solved propagation constant: $\gamma_{z2}/k_0 = j4.27819$.

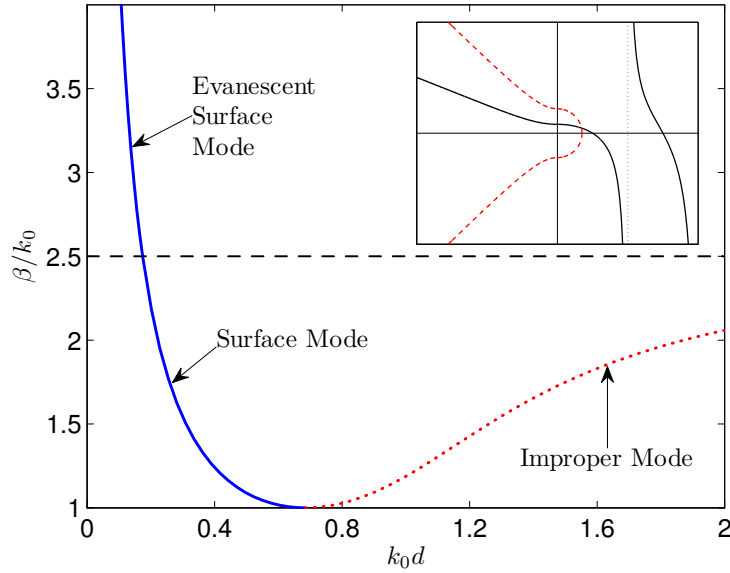
In Figure 4(a), evanescent surface wave mode has low cutoff point. As the electric size increases, the ordinary surface wave mode becomes an evanescent surface wave mode and its effective dielectric constant, ϵ_{eff} , keeps increasing. In Figure 4(b), however, the situation is reversed. The evanescent surface mode has a high cutoff point above which it becomes the ordinary surface wave mode. When k_0d is small, the evanescent surface wave mode has an extremely large ϵ_{eff} that decreases rapidly as the electric size increases. One can refer to the sub-figures of Figure 4 to check its validations, which are graphic solutions shown in earlier section.

3.2.2 Complex Surface Modes and Its Poynting Vectors

It is well known that the complete proper mode spectrum of a lossless DPS dielectric slab include discrete surface wave modes and continuous radiation modes, both of which are real surface wave modes [34, 36]. With a DNG medium, it is proved that all complex roots of the eigen equations



(a) $\epsilon_{r2} = -2.5$, $\mu_{r2} = -0.5$



(b) $\epsilon_{r2} = -2.5$, $\mu_{r2} = -2.5$

Figure 4: Two possible dispersion curves for TE proper surface modes (solid lines) and TE improper leaky modes (dotted lines). The dashed line, representing $\sqrt{\epsilon_{r2}\mu_{r2}}$, is the watershed for evanescent surface mode and ordinary surface modes.

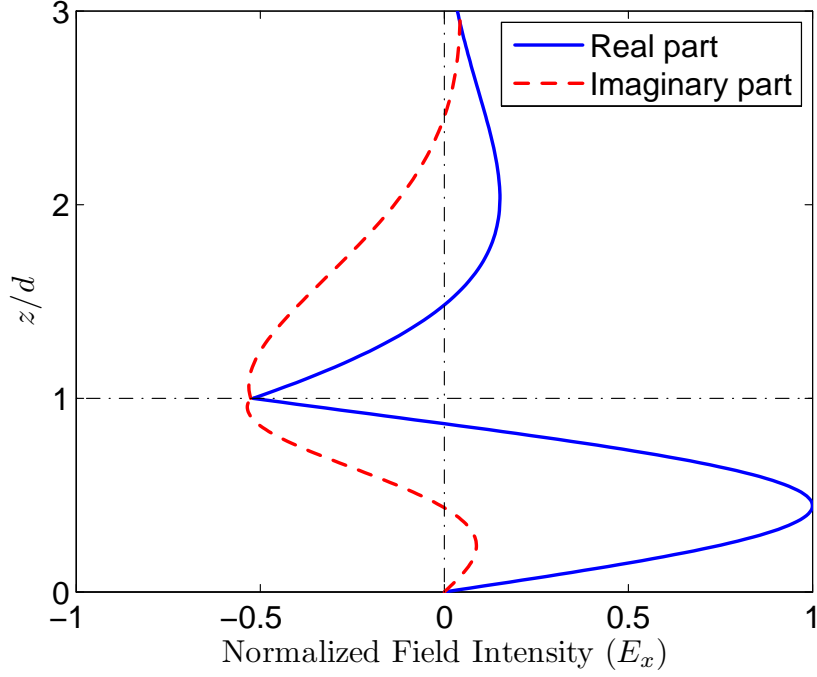


Figure 5: Demonstration of field distribution for a TE complex surface wave mode. Medium and structure parameters are: $\epsilon_{r1} = 1$, $\mu_{r1} = 1$, $\epsilon_{r2} = -2.5$, $\mu_{r2} = -2.5$, $k_0 d = 1.5$ rad. Solved propagation constant: $\gamma_y/k_0 = 0.8261 + j1.1253$.

are on the top Riemann sheet. These solutions, termed complex surface waves, form another set of proper modes. Unlike real surface wave modes, complex surface wave modes have high cutoff electric size, which means that they exist only when $k_0 d$ is small. Therefore, there are an infinite number of complex surface wave modes from very small electric size all the way to large electric size as can be seen later in Figure 7. Figure 5 shows field distribution of a typical complex surface wave mode. The electromagnetic fields decay pretty fast in the air region.

The existence of an infinite number of complex surface wave modes at any frequency seems somehow annoying in terms of suppressing surface wave modes since they will carry away power and lower the radiation efficiency. Fortunately, a careful examination on the Poynting vector eliminates this possibility.

The Poynting vector is defined as

$$\mathbf{S} = \frac{1}{2} \mathbf{E} \times \mathbf{H}^* \quad (28)$$

And we have the following trigonometry identities

$$\sinh(a + jb) = \sinh a \cos b + j \cosh a \sin b \quad (29)$$

$$\cosh(a + jb) = \cosh a \cos b + j \sinh a \sin b \quad (30)$$

$$|\sinh(a + jb)|^2 = \sinh^2 a + \sin^2 b = \frac{1}{2} [\cosh(2a) - \cos(2b)] \quad (31)$$

$$|\cosh(a + jb)|^2 = \cosh^2 a - \sin^2 b = \frac{1}{2} [\cosh(2a) + \cos(2b)] \quad (32)$$

$$\sinh(a + jb) \cosh^*(a + jb) = \frac{1}{2} [\sinh(2a) + j \sin(2b)] \quad (33)$$

$$\sinh^*(a + jb) \cosh(a + jb) = \frac{1}{2} [\sinh(2a) - j \sin(2b)] \quad (34)$$

Using the field components in Section 3.1.6, we have for TE mode

$$S_{y1}^{TE} = -\frac{1}{2} E_{x1} H_{z1}^* = -\frac{\gamma_y^*}{4j\omega\mu_1^*} [\cosh(2\alpha_{z2}d) - \cos(2\beta_{z2}d)] e^{-2\alpha_{z1}(z-d)} e^{-2\alpha y} \quad (35)$$

$$S_{y2}^{TE} = -\frac{1}{2} E_{x2} H_{y2}^* = -\frac{\gamma_y^*}{4j\omega\mu_2^*} [\cosh(2\alpha_{z2}z) - \cos(2\beta_{z2}z)] e^{-2\alpha y} \quad (36)$$

$$S_{z1}^{TE} = \frac{1}{2} E_{x1} H_{y1}^* = -\frac{\gamma_{z1}^*}{4j\omega\mu_1^*} [\cosh(2\alpha_{z2}d) - \cos(2\beta_{z2}d)] e^{-2\alpha_{z1}(z-d)} e^{-2\alpha y} \quad (37)$$

$$S_{z2}^{TE} = \frac{1}{2} E_{x2} H_{y2}^* = \frac{\gamma_{z2}^*}{4j\omega\mu_2^*} [\sinh(2\alpha_{z2}z) + j \sin(2\beta_{z2}z)] e^{-2\alpha y} \quad (38)$$

The total power flow in z -direction for TE mode is

$$\begin{aligned} \frac{P_y^{TE}(y)}{e^{-2\alpha y}} &= \int_0^d S_{y2}^{TE} dz + \int_d^\infty S_{y1}^{TE} dy \\ &= -\frac{\gamma_y^*}{8j\omega\mu_2^*} \left[\frac{\sinh(2\alpha_{z2}d)}{\alpha_{z2}} - \frac{\sin(2\beta_{z2}d)}{\beta_{z2}} \right] - \frac{\gamma_y^*}{8j\omega\mu_1^*\alpha_{z1}} [\cosh(2\alpha_{z2}d) - \cos(2\beta_{z2}d)] \end{aligned} \quad (39)$$

And for TM mode we have

$$S_{y1}^{TM} = \frac{1}{2} E_{y1} H_{x1}^* = \frac{\gamma_y}{4j\omega\epsilon_1} [\cosh(2\alpha_{z2}d) + \cos(2\beta_{z2}d)] e^{-2\alpha_{z1}(z-d)} e^{-2\alpha y} \quad (40)$$

$$S_{y2}^{TM} = \frac{1}{2} E_{z2} H_{x2}^* = \frac{\gamma_y}{4j\omega\epsilon_2} [\cosh(2\alpha_{z2}z) + \cos(2\beta_{z2}z)] e^{-2\alpha y} \quad (41)$$

$$S_{z1}^{TM} = -\frac{1}{2} E_{y1} H_{x1}^* = \frac{\gamma_{z1}}{4j\omega\epsilon_1} [\cosh(2\alpha_{z2}d) + \cos(2\beta_{z2}d)] e^{-2\alpha_{z1}(z-d)} e^{-2\alpha y} \quad (42)$$

$$S_{z2}^{TM} = -\frac{1}{2} E_{z2} H_{x2}^* = -\frac{\gamma_{z2}}{4j\omega\epsilon_2} [\sinh(2\alpha_{z2}z) + j \sin(2\beta_{z2}z)] e^{-2\alpha y} \quad (43)$$

The total power flow in y -direction for TM mode is

$$\begin{aligned} \frac{P_y^{TM}(y)}{e^{-2\alpha y}} &= \int_0^d S_{y2}^{TM} dz + \int_d^\infty S_{y1}^{TM} dz \\ &= \frac{\gamma_y}{8j\omega\epsilon_2} \left[\frac{\sinh(2\alpha_{z2}d)}{\alpha_{z2}} + \frac{\sin(2\beta_{z2}d)}{\beta_{z2}} \right] + \frac{\gamma_y}{8j\omega\epsilon_1\alpha_{z1}} [\cosh(2\alpha_{z2}d) + \cos(2\beta_{z2}d)] \end{aligned} \quad (44)$$

Although the equations of the total power flow (39) and (44) are quite complicated, the result turns out to be simply zero [37] as can be seen by the following physical argument. To give out a clear picture of the power flow density, the Poynting vector is drawn in Figure 6. Dotted lines are the boundaries of a conjectured box with dimension of $4 \text{ mm} \times 20 \text{ mm}$. The power flow has different directions in the air and inside the dielectric layer. The average total power flowing out of the box via the left and right side walls is equal to the power flowing into the box from the top wall. Now assuming the top wall is moved to infinity, there is no power flowing into the box from the top wall since the complex surface modes have zero fields at infinity. According to the energy conservation law, the power exchange via the left side wall $P_{y1} = \int_0^\infty S_{y1}(z, y) dz$ must be equal to the power exchange via the right side wall $P_{y2} = \int_0^\infty S_{y2}(z, y) dz$. Note that the propagation constant along y -direction is now a complex number $\gamma_y = \alpha + j\beta$ where $\alpha \neq 0$, and P_1 and P_2 are related by $P_2 = P_1 e^{-2\alpha(y_2 - y_1)}$. To ensure $P_1 = P_2$, the only possibility is $P_1 = P_2 = 0$. Thus all the complex surface modes have zero power flow in y -direction. They do not transport any energy.

3.3 Mode Spectrum of DNG Medium

As discussed in previous section, now we have got the eigen equations of transverse electric (TE) and transverse magnetic (TM) modes for waves propagating in ρ -direction:

$$\frac{\mu_{r2}}{\gamma_{z2}} \sinh(\gamma_{z2}d) + \frac{\mu_{r1}}{\gamma_{z1}} \cosh(\gamma_{z2}d) = 0 \quad \text{TE mode} \quad (45)$$

$$\frac{\gamma_{z2}}{\epsilon_{r2}} \sinh(\gamma_{z2}d) + \frac{\gamma_{z1}}{\epsilon_{r1}} \cosh(\gamma_{z2}d) = 0 \quad \text{TM mode} \quad (46)$$

$$\gamma_{zi} = \pm \sqrt{-k_0^2 \epsilon_{ri} \mu_{ri} - \gamma_\rho^2} = \alpha_{zi} + j\beta_{zi} \quad (47)$$

where γ_{zi} ($i = 1, 2$) is the complex propagation constant along z -direction in Region I and II, and $\gamma_\rho \hat{\rho} = \gamma_x \hat{x} + \gamma_y \hat{y} = (\alpha + j\beta) \hat{\rho}$ is the propagation constant in xy -plane. Due to the double-valued nature of the square root in the expression for γ_{zi} , mathematically there exist two types of solutions: one has a positive real part of γ_{z1} resulting in a zero field at infinity, and the other has a negative real part of γ_{z1} resulting in an infinitely large field at infinity. Physically, only the first group can

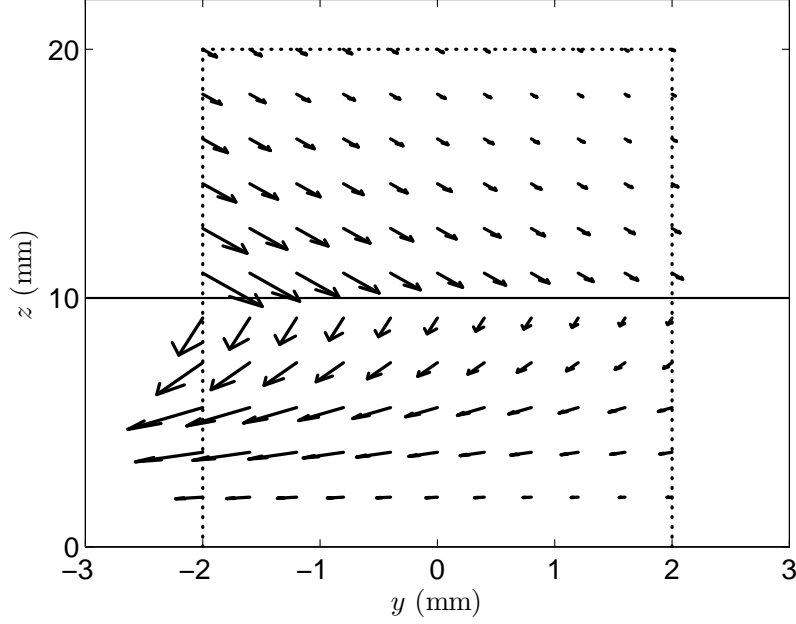
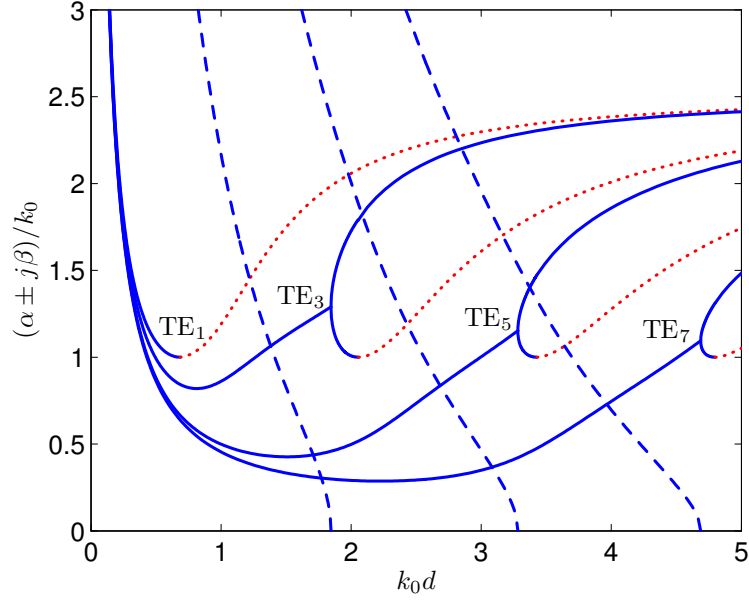


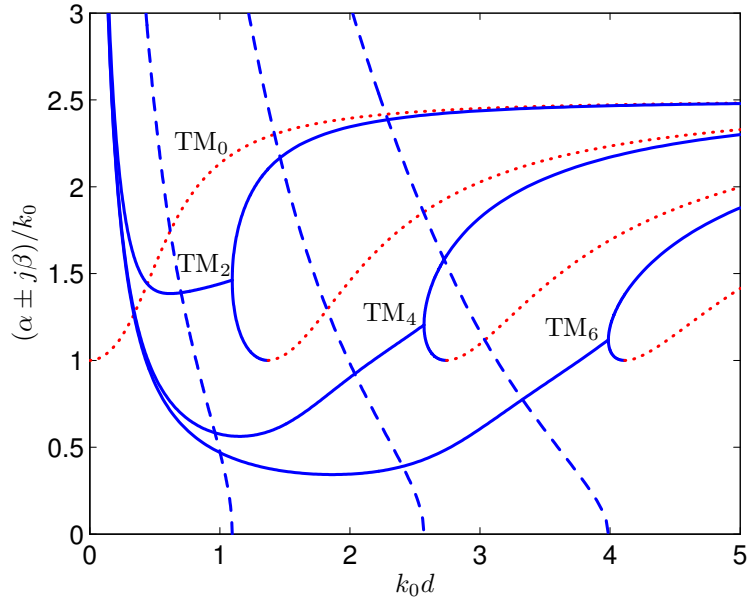
Figure 6: The Poynting vector of a TE complex mode. Dotted lines are the boundary of a conjectured box. Solid line is the interface of the dielectric slab and the air. The medium and structure parameters are: $\epsilon_{r1} = 1$, $\mu_{r1} = 1$, $\epsilon_{r2} = -2.5$, $\mu_{r2} = -2.5$, $d = 0.01$ m, $k_0 = 100$ rad/m. Solved propagation constant: $\gamma_y/k_0 = 2.09195 + j0.86938$.

exist. However, this by no means implies that the second group has little value. In fact, the second group is important in both mathematical manipulations and real applications as leaky waves to be discussed in detail in next section [38].

As described in detail in [27] and listed in Table 1, a conventional lossless DPS has only two types of proper eigenmodes: a finite number of discrete ordinary real surface modes, and continuous radiation modes, and any field solutions can be expressed as the superposition of these two kinds of modes. With DNG media, the mode set becomes much more complicated. In addition to discrete ordinary surface modes and continuous radiation modes, two discrete surface modes (evanescent real modes and complex modes), are also part of its complete mode spectrum. Furthermore, unlike in DPS media that have only a finite number of discrete surface wave modes, the DNG media have an infinite number of discrete complex modes that further complicate mode solutions [27, 39].



(a) TE modes



(b) TM modes

Figure 7: Dispersion diagrams for all modes. Solid lines are for normalized β of the proper modes. Dashed lines are for normalized α of the proper modes. Dotted lines are for normalized β of the improper modes. The medium parameters are: $\epsilon_{r1} = 1$, $\mu_{r1} = 1$, $\epsilon_{r2} = -2.5$, $\mu_{r2} = -2.5$.

Table 1: Complete mode spectrum for dielectric slab (DPS and DNG).

| Spectrum | DPS | DNG |
|--|-----------------|-----------------|
| Discrete evanescent real surface mode $\alpha = 0, (\beta/k_0)^2 > \epsilon_{r2}\mu_{r2}$ | Improper | Proper |
| Discrete ordinary real surface mode $\alpha = 0, \epsilon_{r1}\mu_{r1} < (\beta/k_0)^2 < \epsilon_{r2}\mu_{r2}$ | Proper/Improper | Proper/Improper |
| Continuous radiation mode $\alpha = 0, -\infty < (\beta/k_0)^2 < \epsilon_{r1}\mu_{r1}$ | Proper | Proper |
| Discrete complex surface mode $\alpha \neq 0, \beta \neq 0$ | Improper | Proper |

3.4 Dispersion Diagrams and Power Flow

Figure 7 shows dispersion diagrams for both TE and TM modes for a DNG slab, including evanescent, ordinary, and complex surface modes. Also included are real improper modes drawn as dotted lines. When the electric size of the dielectric slab is much smaller than the cutoff electric size of the first real mode, all complex modes exist with very high normalized α and β , or in terms of wave properties, very high attenuation and very slow phase velocity. As the k_0d increases, β/k_0 tends to decrease rapidly within a very narrow range followed by a steady increase until its cutoff point. Notice that it is not monotonic and the value of β/k_0 can be less than unity (so called fast wave), a notable difference compared with real surface modes in a DPS medium. The curve of α/k_0 , however, monotonically decreases very fast as k_0d increases. At the cutoff point, α reaches zero and β becomes the starting point of a real mode. The real surface mode bifurcates into two branches from the cutoff point. One branch has an increasing β/k_0 as k_0d becomes bigger while the other has a decreasing β/k_0 . The branch with an decreasing β/k_0 will reach unity shortly. Further increasing electric size makes β/k_0 of the second branch begin to rise. However, it is no longer a proper mode. Note that the figures are plotted as functions of normalized electrical dimension of the slab and we keep using k_0d instead of frequency. Thus the above argument can be used for inherently dispersive DNG metamaterials, as long as one interprets them as fixed operating frequency while the layer thickness is changing.

As a comparison, the dispersion diagram of a DPS slab is plotted in Figure 8. Note that there is no cutoff for TM_0 mode and all dispersion curves are monotonic increasing as the electric size increases.

From the above results, even for ordinary real surface modes, DNG media impose a lot of difficulties by introducing a bifurcation near its cutoff frequency. A typical dispersion curve of TE_3

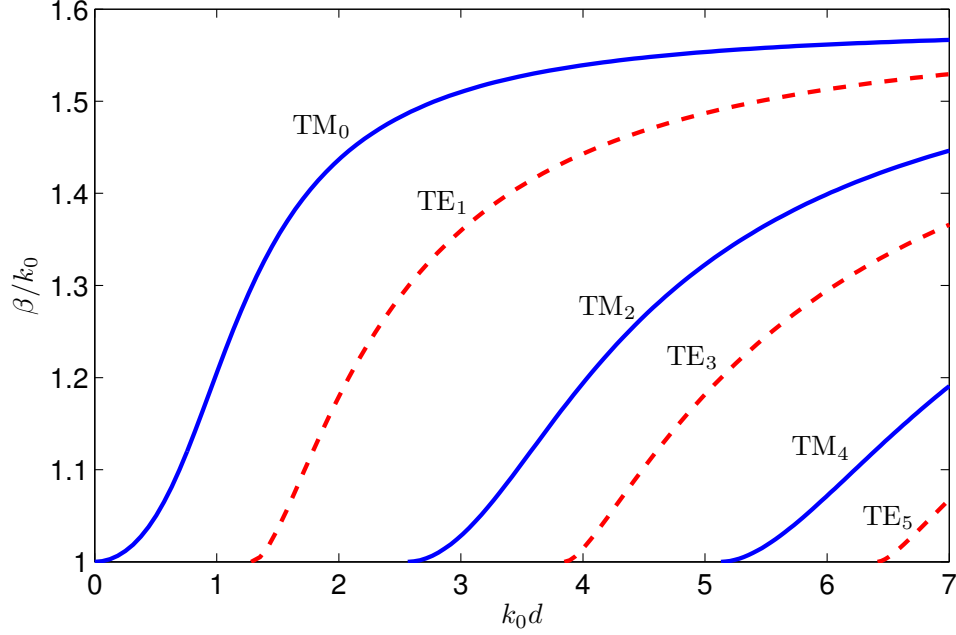


Figure 8: Dispersion diagram of TE modes (dashed lines) and TM modes (solid lines) for double positive material. The medium parameters are: $\epsilon_{r1} = 1$, $\mu_{r1} = 1$, $\epsilon_{r2} = 2.5$, $\mu_{r2} = 1$.

mode is shown in Fig. 9(a), along with its power flow in Fig. 9(b). From Fig. 9(a), it is seen that only a complex mode exists (branch ‘A’) when k_0d is lower than its cutoff threshold. As shown in Section 3.2, the zero power flow in Fig. 9(b) shows that the complex surface mode does not carry away power in ρ -direction as proved in [27]. With the electric size continuing to increase, two real surface modes show up from the cutoff point. The top branch (branch ‘B’) has a negative power flow (power flow direction is opposite to the wave propagation direction) and shows backward properties. When a waveguide operates at this mode, its fields largely are confined inside the dielectric layer. The bottom branch (branch ‘C’) has a positive power flow and its fields extend far away in the air region. When a waveguide operates at this mode, it does not exhibit backward properties. Further increasing the electric size causes the fields in the air region to decay even more slowly and eventually reach infinity. At that point, the radiation boundary conditions are violated and the mode becomes improper.

As a comparison, the TE_3 mode of a conventional double positive medium has a much simpler dispersion curve, *i.e.*, showing up at the cutoff point and monotonically approaching the limit of $\sqrt{\epsilon_{r2}\mu_{r2}}$. Readers who are interested in detailed derivations and comparisons between DPS medium

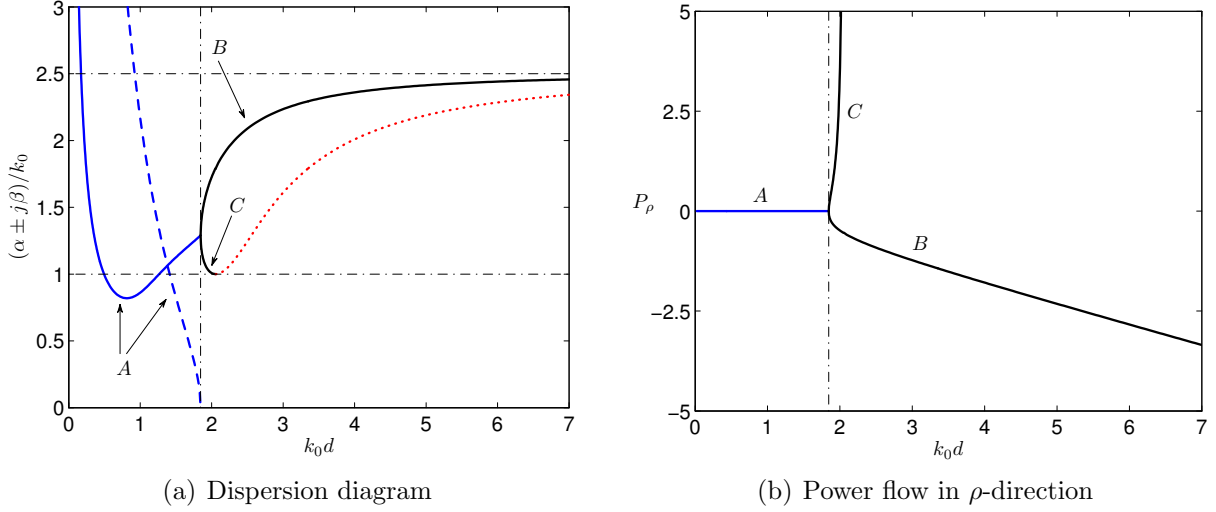


Figure 9: Dispersion diagram and the power flow in ρ -direction for TE₃ mode. ‘A’ is for complex surface mode; ‘B’ is for top branch of the real surface mode; ‘C’ is for bottom branch of the real surface mode. The medium parameters are: $\epsilon_{r1} = 1$, $\mu_{r1} = 1$, $\epsilon_{r2} = -2.5$, $\mu_{r2} = -2.5$.

and DNG medium are directed to [27, 36].

3.5 The Leaky Modes

Tamir and Kou studied leaky waves (complex waves) in an asymmetric slab [40] as shown in Figure 10, which the top and bottom half-spaces are different. They claim that there are eight different leaky waves guided by an asymmetric layer configuration, but only four of the eight can be excited in conventional DPS materials. Those eight leaky waves can be divided as four forward and four backward leaky waves, or four co- and four contra-leaky waves as shown in Fig. 11. By co-leaky waves it is meant that the fields in both regions (top and bottom half-spaces) increase or decrease exponentially. The contra-leaky waves mean that the field in one region increases exponentially, while the field in another region decreases exponentially. The distance between the arrows is inversely proportional to the field magnitude. It is found that for a lossless DPS grounded slab, there are only two improper complex modes (leaky waves). If the slab is lossy, the conventional surface wave modes become complex modes, which are called leaky waves by Tamir and Kou. A plasma slab (negative ϵ) will add another type of proper complex modes (infinite number of discrete complex modes) even the plasma is lossless. For a grounded DNG slab only two proper complex modes exist for a lossless slab. If the slab is lossy, the proper surface wave modes may become proper complex modes or improper complex modes.

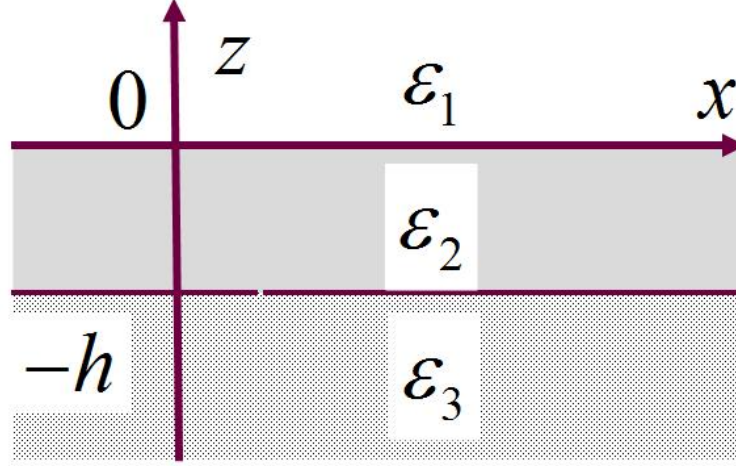


Figure 10: Diagram for an asymmetric slab (top and bottom half-spaces are different).

Figure 12 shows the leaky waves for a symmetric or grounded slab with double positive (DPS) or double negative (DNG) materials. Tx or Bx for poles (modes) on top or bottom Riemann sheet, x stands for which quadrant (1st to 4th). Forward and backward: forward wave or backward wave. It is found that for a lossless DPS grounded slab, there are only two improper complex modes (leaky waves) on B4 and B3. If the slab is lossy, the conventional surface wave modes become complex modes on T4, which are called as leaky waves by Tamir and Kou. A plasma slab (negative ϵ) will add another type of proper complex modes. For a DNG slab, there are proper complex modes on T3 and T4 for both lossless and lossy slab.

For a grounded slab with DNG materials, only two proper complex modes exist for a lossless slab. If the slab is lossy, the proper surface wave modes may become proper complex modes or improper complex modes. For a complete mode spectrum, please refer to Table 2.

3.6 Mode Loci vs. Frequency/Thickness

Knowing mode distributions and behaviors in the complex γ_ρ -plane is important in solving dielectric waveguide problems, excitation problems, and microwave strip problems. It provides an initial guess when using Newton's method to find solutions. In performing Sommerfeld integrations, we resort to mode loci to conceive a proper integral path which is an essential step in solving an excitation problem. In this and next sub-sections, we will first examine how complex modes change as

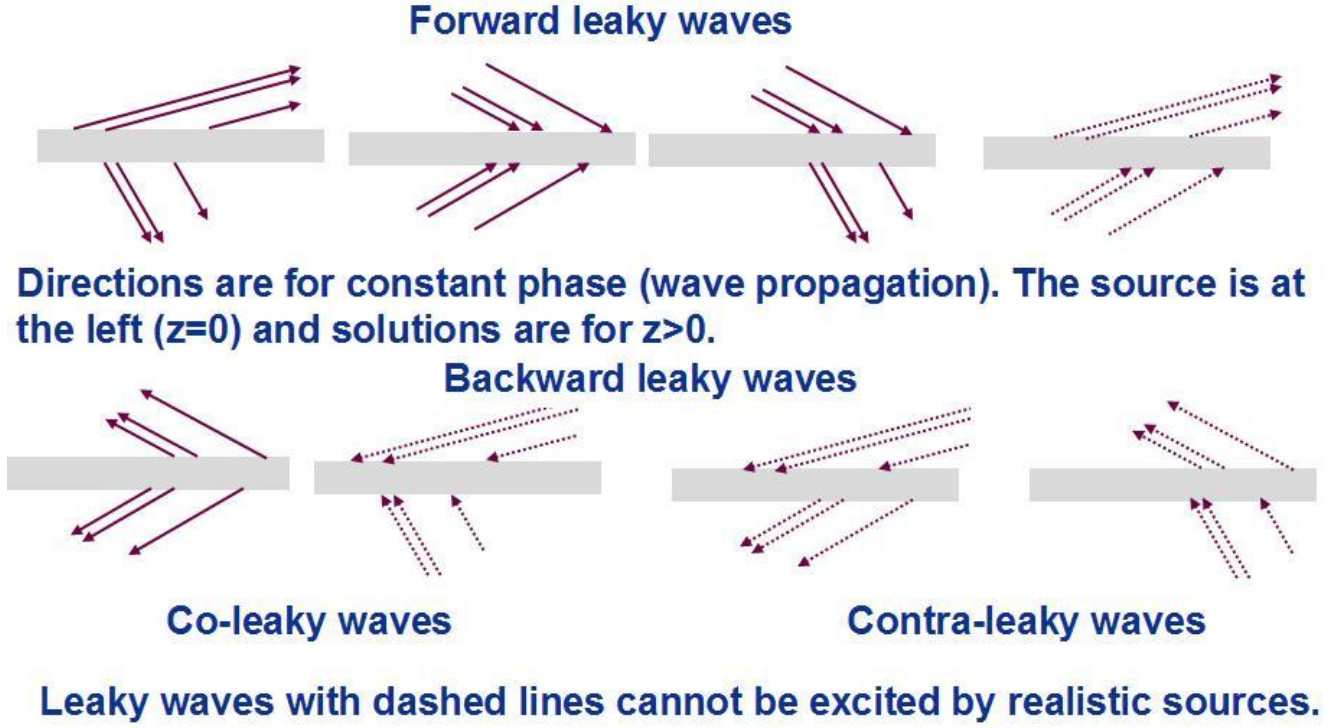


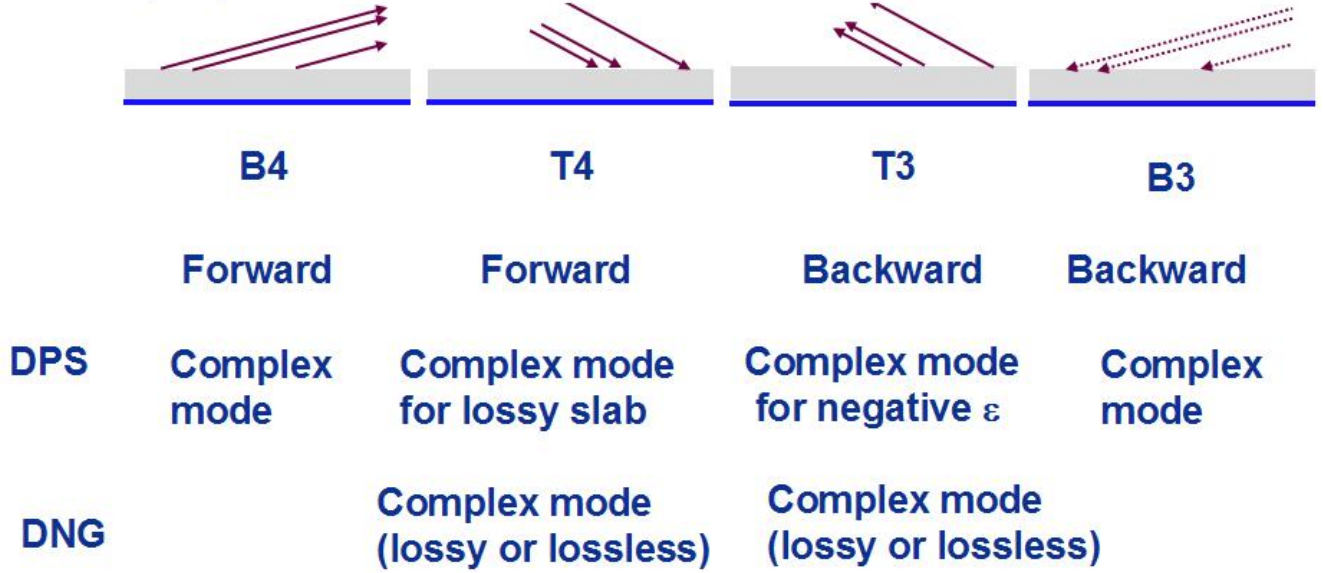
Figure 11: Leaky waves in an asymmetric slab as shown in Figure 10. The distance between the arrows is inversely proportional to the field magnitude.

Table 2: Complete Spectrum of Dielectric Slab

| Modes | | Finite number, discrete evanescent surface mode | Finite number, discrete normal surface mode | Infinite number, discrete complex mode | Continuous mode |
|---------------------|----|---|---|--|-----------------|
| DPS (TE, TM) | | Improper | Proper/impr. | Improper | Proper |
| Negative ϵ | TE | Improper | None | Improper | Proper |
| | TM | Proper | None | Proper | Proper |
| Negative μ | TE | Proper | None | Proper | Proper |
| | TM | Improper | None | Improper | Proper |
| DNG (TE, TM) | | Proper | Proper/impr. | Proper | Proper |

the electric size $k_0 d$ varies. Later we will study mode loci in lossy medium.

Directions are for constant phase (wave propagation). The source is at the left ($z=0$) and solutions are for $z>0$.



For a given source, all modes carry the power away from the source.

Figure 12: Leaky waves in a symmetric or grounded slab for both double positive (DPS) and double negative (DNG) materials. Tx or Bx for poles (modes) on top or bottom Riemann sheet, x stands for which quadrant (1st to 4th). Forward and backward: forward wave or backward wave. For a DPS slab, there are improper complex modes on B4 and B3. If the slab is lossy, the proper complex modes may exist on T4. For a DNG slab, there are proper complex modes on T3 and T4 for both lossless and lossy slab.

For the most general case, the propagation constants are assumed to be complex as shown in (47). The equations $\gamma_{zi}^2 = -k_0^2 \epsilon_{ri} \mu_{ri} - \gamma_\rho^2$ ($i = 1, 2$ for Region I or II) are functions of γ_ρ^2 , therefore given $\gamma_\rho = \alpha + j\beta$ a solution, $-\gamma_\rho$ is also a solution. After some algebra operations, we have [39]

$$\alpha_{z1}^2 - \beta_{z1}^2 + 2j\alpha_{z1}\beta_{z1} = -k_1^2 - \alpha^2 + \beta^2 - 2j\alpha\beta \quad (48)$$

$$\alpha_{z2}^2 - \beta_{z2}^2 + 2j\alpha_{z2}\beta_{z2} = -k_2^2 - \alpha^2 + \beta^2 - 2j\alpha\beta \quad (49)$$

where $k_i^2 = k_0^2 \epsilon_{ri} \mu_{ri}$ ($i = 1, 2$). To satisfy the equations for the imaginary part, one must have

$$\alpha_{z1}\beta_{z1} = \alpha_{z2}\beta_{z2} = -\alpha\beta \quad (50)$$

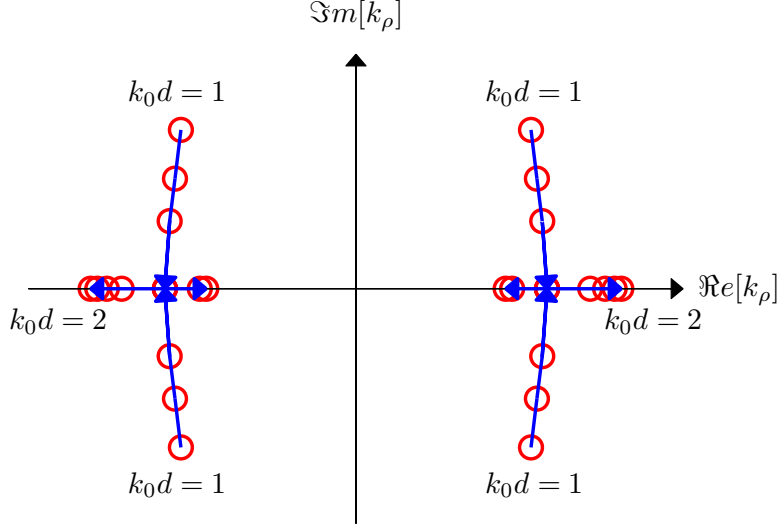


Figure 13: TM₂ pole loci as the normalized thickness k_0d increases. Medium parameters are: $\epsilon_{r1} = 1$, $\mu_{r1} = 1$, $\epsilon_{r2} = -2.5$, $\mu_{r2} = -1.6$, k_0d increases from 1 to 2.

Table 3: Possible sign choices of complex modes for lossless medium.

| | γ | γ^* | $-\gamma^*$ | $-\gamma$ |
|-----------------------------|-------------------------|-------------------------|-------------------------|-------------------------|
| (α, β) | $(+, +)$ | $(+, -)$ | $(-, +)$ | $(-, -)$ |
| $(\alpha_{z1}, \beta_{z1})$ | $(+, -)$ | $(+, +)$ | $(+, +)$ | $(+, -)$ |
| $(\alpha_{z2}, \beta_{z2})$ | $(+, -)$ or $(-, +)$ | $(+, +)$ or $(-, -)$ | $(+, +)$ or $(-, -)$ | $(+, -)$ or $(-, +)$ |

Simultaneously changing the sign of β and β_{z1} does not violate the above transcendental eigenequations [39]. Therefore, γ_ρ^* is also a solution. If γ_ρ^* is a solution, from the previous argument we can conclude that $-\gamma_\rho^*$ is a solution as well. Table 3 lists the possible sign choices for a lossless medium. The first two columns are solutions for outward waves and the last two columns are solutions for inward waves. Those sign choices are very helpful to understand the behaviors of complex waves. For example, for the outward waves shown in the first two columns, β_{z1} has opposite sign of β . The wave propagates in a combining $+\rho/-z$ direction or a $-\rho/+z$ direction.

When electric size is small, only complex modes exist. According to the above conclusion, complex modes always form a quartet for lossless media. Fig. 13 shows a particular mode TM₂. With electric size increasing, complex poles keep moving toward the real axis and become the starting point of the bifurcated real modes. One of the two branches moves inward, touches the

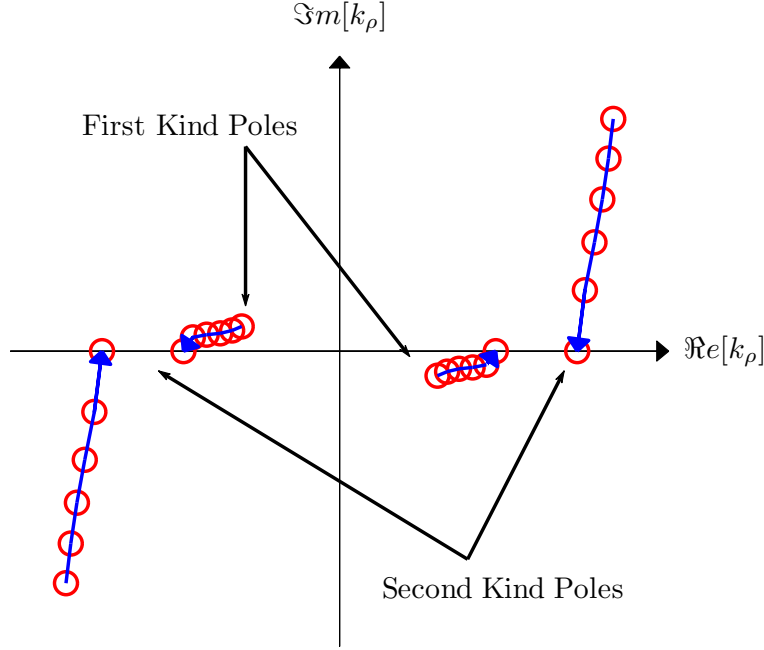


Figure 14: TM_2 real pole loci as loss tangent δ decreases from 0.4 to 0 with step size 0.08. Medium parameters are: $\epsilon_{r1} = 1$, $\mu_{r1} = 1$, $\epsilon_{r2} = -2.5(1 + j\delta)$, $\mu_{r2} = -1.6$, $k_0d = 1.6$.

branch point at $k_0d = \pi/\sqrt{3} = 1.8138$ for the parameters given in Fig. 13, and eventually becomes improper mode. Meanwhile the other branch moves outward and approaches to $\sqrt{\epsilon_{r2}\mu_{r2}}k_0$. This behavior is also well-expected from the dispersion curve in Fig. 9(a). The same comments are also applied to all other modes shown in Fig. 7 except TE_1 and TM_0 , because they are not complex modes for any electric size.

3.7 Mode Loci vs. Loss

In solving for the Green's function of layered media or other excitation problems, electromagnetic fields are often represented as Sommerfeld integrals [31,32]. A detailed discussion about Sommerfeld integral is presented in next chapter. When performing integral evaluations, one needs to specify the integral path. There is no problem for a lossy medium because all the surface wave poles are off the real axis, and the inverse Fourier transform along the real axis converges due to the loss. For a lossless medium, it is not straightforward to conceive a proper integral path because the integrand blows up near poles in the real axis. [31] has a detailed analysis of Sommerfeld integral path (SIP) for conventional lossless DPS material. In short, we assume a lossy medium first, then monitor

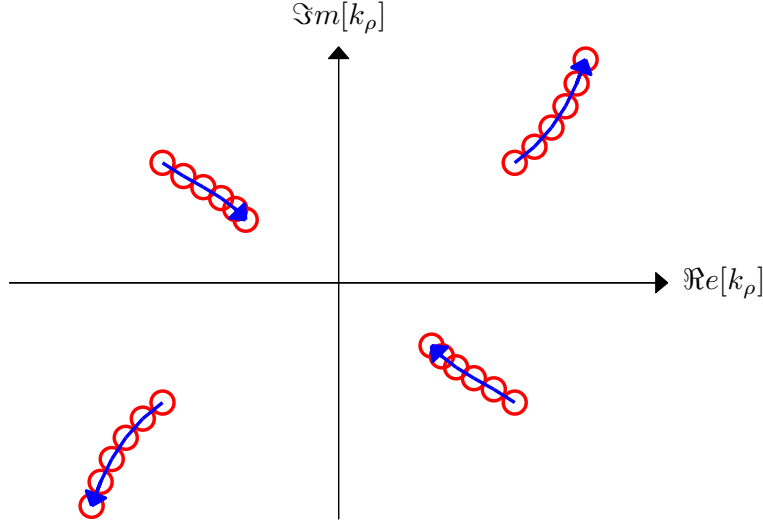


Figure 15: TM₂ complex pole loci as loss tangent δ increases from 0 to 0.4 with step size 0.08. Medium parameters are: $\epsilon_{r1} = 1$, $\mu_{r1} = 1$, $\epsilon_{r2} = -2.5(1 + j\delta)$, $\mu_{r2} = -1.6$, $k_0d = 1$.

how poles change as loss becomes smaller and smaller, and finally construct an integral path that does not encounter any poles. However, when dealing with DNG material, we cannot use exactly the same SIP as we do for conventional DPS material. Attention has to be paid to how different kinds of poles change as the DNG medium loss approaches zero.

Fig. 14 shows TM₂ pole loci when loss becomes smaller and smaller. The blue arrows show the direction of decreasing loss. There are two kinds of surface wave modes. The first one has most of its power flow in the air while the other has most of its power flow in the dielectric layer. When the medium is lossy, the first kind of surface wave poles are in the second and fourth quadrants, and the second kind of surface wave poles are in the first and third quadrants. As the loss approaches zero, both merge to real axis.

Fig. 15 shows complex pole loci versus the medium loss. The blue arrows show the direction of increasing loss. There are several observations: First, unlike the lossless medium where γ , $-\gamma$, γ^* , and $-\gamma^*$ are all solutions, only γ and $-\gamma$ are solutions. Second, as the loss becomes larger, one pair of complex poles become faster and attenuate less (decreasing β and α), and the others become slower and attenuate more (increasing β and α). This information may be used in designing leaky wave antenna with a large aperture with relative uniform field distributions.

4 Sommerfeld Integral Path and Numerical Considerations

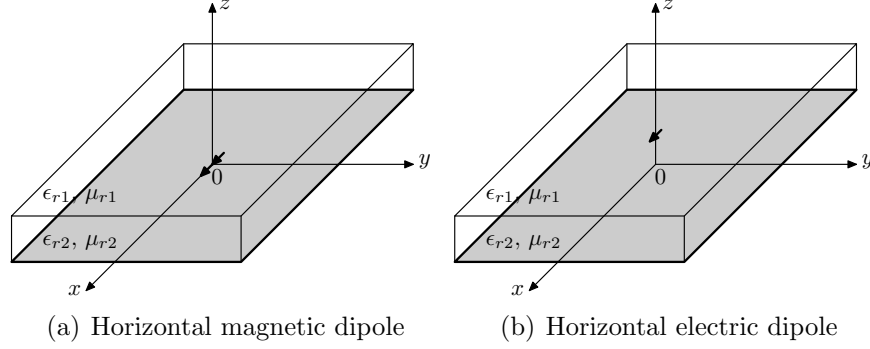


Figure 16: Horizontal magnetic dipole on PEC covered with DNG media and horizontal electric dipole at the interface of grounded DNG media and air.

So far we have studied eigenproblems of grounded dielectric slabs of DNG media. When a finite source such as shown in Fig. 16 is considered, the spectral domain approach is widely used. At the very beginning of this section, we will introduce spectral domain approach. The HMD case (configured as Fig. 16(a)) is solved as an example of this approach. It is found that the solutions are expressed via a Green's function. In a layered medium, the Green's function is written as a Sommerfeld-type integral [31], whose integrand has poles on the k_ρ -plane that correspond to the eigenmode solutions of the same structure with source removed. In the rest of this section, a detailed discussion about Sommerfeld Integral Path is presented.

4.1 Spectral Domain Approach

4.1.1 Hertz Potentials

The Hertz potentials are defined as

$$\mathbf{E}^h = -j\omega\mu\nabla \times \mathbf{\Pi}^h \quad (51)$$

$$\mathbf{H}^e = j\omega\epsilon\nabla \times \mathbf{\Pi}^e \quad (52)$$

In source free and homogeneous isotropic region, both $\mathbf{\Pi}_e$ and $\mathbf{\Pi}_h$ satisfy the homogeneous vector Helmholtz equation

$$(\nabla^2 + k_i^2) \mathbf{\Pi}_i^{e,h} = 0 \quad (53)$$

In a layered structure whose material constants are only functions of z , the electromagnetic fields are decoupled to TE^{*z*} ($\mathbf{\Pi}^e = 0$, $\mathbf{\Pi}^h = \Pi^{hz}\hat{\mathbf{z}}$) and TM^{*z*} ($\mathbf{\Pi}^e = \Pi^{ez}\hat{\mathbf{z}}$, $\mathbf{\Pi}^h = 0$) modes [31]. Thus Equation (53) is reduced to homogeneous scalar Helmholtz equation whose cylindrical form is

$$\left[\frac{1}{\rho} \frac{\partial}{\partial \rho} \left(\rho \frac{\partial}{\partial \rho} \right) + \frac{1}{\rho^2} \frac{\partial^2}{\partial \phi^2} + \frac{\partial^2}{\partial z^2} + k_i^2 \right] \Pi^{ez,hz} = 0 \quad (54)$$

4.1.2 Fourier Transforms

Given that the Hertz potentials are solved, the electric and magnetic fields are found by

$$\mathbf{E} = \nabla \times \nabla \times \mathbf{\Pi}^e - j\omega\mu\nabla \times \mathbf{\Pi}^h = k^2\mathbf{\Pi}^e + \nabla\nabla \cdot \mathbf{\Pi}^e - j\omega\mu\nabla \times \mathbf{\Pi}^h \quad (55)$$

$$\mathbf{H} = \nabla \times \nabla \times \mathbf{\Pi}^h + j\omega\epsilon\nabla \times \mathbf{\Pi}^e = k^2\mathbf{\Pi}^h + \nabla\nabla \cdot \mathbf{\Pi}^h + j\omega\epsilon\nabla \times \mathbf{\Pi}^e \quad (56)$$

Taking the advantage of the symmetry of the problem, the Fourier transforms adopted by [43] are used. They are

$$\Pi^{ez}(\rho, \phi, z) = -2j\pi \sin \phi \int_0^\infty \tilde{F}_e(\lambda^2, z) J_1(k_0\lambda\rho) d\lambda \quad (57)$$

$$\Pi^{hz}(\rho, \phi, z) = -2j\pi \cos \phi \int_0^\infty \tilde{F}_h(\lambda^2, z) J_1(k_0\lambda\rho) d\lambda \quad (58)$$

With such Fourier transforms, (54) is converted to 1-D differential equation

$$\left[\frac{d^2}{dz^2} - \gamma_{zi}^2 \right] \tilde{F}_{e,h}(\lambda, z) = 0 \quad (59)$$

where $\gamma_{zi}^2 = k_0^2\lambda^2 - k_i^2 = k_0^2(\lambda^2 - \epsilon_{ri}\mu_{ri})$. Notice that $\lambda = k_\rho/k_0$ is normalized transverse wavenumber.

4.1.3 TE Fields in Cylindrical Coordinate

The fields of TE modes in spectrum domain are

$$E_\rho = -j\omega\mu \frac{1}{\rho} \frac{\partial \Pi^{hz}}{\partial \phi} = 2\pi\omega\mu \sin \phi \int_0^\infty \tilde{F}_h(\lambda^2, z) \frac{J_1(k_0\lambda\rho)}{\rho} d\lambda \quad (60a)$$

$$E_\phi = j\omega\mu \frac{\partial \Pi^{hz}}{\partial \rho} = 2\pi\omega\mu \cos \phi \int_0^\infty \tilde{F}_h(\lambda^2, z) \left[k_0\lambda J_0(k_0\lambda\rho) - \frac{J_1(k_0\lambda\rho)}{\rho} \right] d\lambda \quad (60b)$$

$$E_z = 0 \quad (60c)$$

$$H_\rho = \frac{\partial^2 \Pi^{hz}}{\partial \rho \partial z} = -2j\pi \cos \phi \int_0^\infty \tilde{F}_h'(\lambda^2, z) \left[k_0\lambda J_0(k_0\lambda\rho) - \frac{J_1(k_0\lambda\rho)}{\rho} \right] d\lambda \quad (60d)$$

$$H_\phi = \frac{1}{\rho} \frac{\partial^2 \Pi^{hz}}{\partial \phi \partial z} = 2j\pi \sin \phi \int_0^\infty \tilde{F}_h'(\lambda^2, z) \frac{J_1(k_0\lambda\rho)}{\rho} d\lambda \quad (60e)$$

$$\begin{aligned} H_z &= \left(\frac{\partial^2}{\partial z^2} + k^2 \right) \Pi^{hz} = -2j\pi \cos \phi \int_0^\infty \left[\tilde{F}_h''(\lambda^2, z) + k^2 \tilde{F}_h(\lambda^2, z) \right] J_1(k_0\lambda\rho) d\lambda \\ &= -2j\pi k_0^2 \cos \phi \int_0^\infty \lambda^2 \tilde{F}_h(\lambda^2, z) J_1(k_0\lambda\rho) d\lambda \end{aligned} \quad (60f)$$

where $\tilde{F}_h'(\lambda^2, z)$ and $\tilde{F}_h''(\lambda^2, z)$ are the first and second order derivatives with respect to z .

In deriving the above formula, the following identity is used

$$\frac{dJ_1(k_0\lambda\rho)}{d\rho} = \frac{1}{\rho} [k_0\lambda\rho J_0(k_0\lambda\rho) - J_1(k_0\lambda\rho)] \quad (61)$$

When $\rho = 0$, we have $\lim_{\rho \rightarrow 0} \frac{J_1(k_0\lambda\rho)}{\rho} = \frac{k_0\lambda}{2}$, the above formulas are simplified to

$$E_\rho = 2\pi\omega\mu \sin \phi \int_0^\infty \tilde{F}_h(\lambda^2, z) \frac{k_0\lambda}{2} d\lambda \quad (62a)$$

$$E_\phi = 2\pi\omega\mu \cos \phi \int_0^\infty \tilde{F}_h(\lambda^2, z) \frac{k_0\lambda}{2} d\lambda \quad (62b)$$

$$E_z = 0 \quad (62c)$$

$$H_\rho = -2j\pi \cos \phi \int_0^\infty \tilde{F}_h'(\lambda^2, z) \frac{k_0\lambda}{2} d\lambda \quad (62d)$$

$$H_\phi = 2j\pi \sin \phi \int_0^\infty \tilde{F}_h'(\lambda^2, z) \frac{k_0\lambda}{2} d\lambda \quad (62e)$$

$$H_z = 0 \quad (62f)$$

4.1.4 TM Fields in Cylindrical Coordinate

The fields of TM modes in spectrum domain are

$$E_\rho = \frac{\partial^2 \Pi^{ez}}{\partial \rho \partial z} = -2j\pi \sin \phi \int_0^\infty \tilde{F}_e'(\lambda^2, z) \left[k_0 \lambda J_0(k_0 \lambda \rho) - \frac{J_1(k_0 \lambda \rho)}{\rho} \right] d\lambda \quad (63a)$$

$$E_\phi = \frac{1}{\rho} \frac{\partial^2 \Pi^{ez}}{\partial \phi \partial z} = -2j\pi \cos \phi \int_0^\infty \tilde{F}_e'(\lambda^2, z) \frac{J_1(k_0 \lambda \rho)}{\rho} d\lambda \quad (63b)$$

$$\begin{aligned} E_z &= \left(\frac{\partial^2}{\partial z^2} + k^2 \right) \Pi^{ez} = -2j\pi \sin \phi \int_0^\infty \left[\tilde{F}_e''(\lambda^2, z) + k^2 \tilde{F}_e(\lambda^2, z) \right] J_1(k_0 \lambda \rho) d\lambda \\ &= -2j\pi k_0^2 \sin \phi \int_0^\infty \lambda^2 \tilde{F}_e(\lambda^2, z) J_1(k_0 \lambda \rho) d\lambda \end{aligned} \quad (63c)$$

$$H_\rho = j\omega\epsilon \frac{1}{\rho} \frac{\partial \Pi^{ez}}{\partial \phi} = 2\pi\omega\epsilon \cos \phi \int_0^\infty \tilde{F}_e(\lambda^2, z) \frac{J_1(k_0 \lambda \rho)}{\rho} d\lambda \quad (63d)$$

$$H_\phi = -j\omega\epsilon \frac{\partial \Pi^{ez}}{\partial \rho} = -2\pi\omega\epsilon \sin \phi \int_0^\infty \tilde{F}_e(\lambda^2, z) \left[k_0 \lambda J_0(k_0 \lambda \rho) - \frac{J_1(k_0 \lambda \rho)}{\rho} \right] d\lambda \quad (63e)$$

$$H_z = 0 \quad (63f)$$

where $\tilde{F}_h'(\lambda^2, z)$ and $\tilde{F}_h''(\lambda^2, z)$ are the first and second order derivatives with respect to z .

When $\rho = 0$, we have

$$E_\rho = -2j\pi \sin \phi \int_0^\infty \tilde{F}_e'(\lambda^2, z) \frac{k_0 \lambda}{2} d\lambda \quad (64a)$$

$$E_\phi = -2j\pi \cos \phi \int_0^\infty \tilde{F}_e'(\lambda^2, z) \frac{k_0 \lambda}{2} d\lambda \quad (64b)$$

$$E_z = 0 \quad (64c)$$

$$H_\rho = 2\pi\omega\epsilon \cos \phi \int_0^\infty \tilde{F}_e(\lambda^2, z) \frac{k_0 \lambda}{2} d\lambda \quad (64d)$$

$$H_\phi = -2\pi\omega\epsilon \sin \phi \int_0^\infty \tilde{F}_e(\lambda^2, z) \frac{k_0 \lambda}{2} d\lambda \quad (64e)$$

$$H_z = 0 \quad (64f)$$

4.1.5 Rewriting as Infinite Integrals

Equation (60) and (63) are integrals from 0 to ∞ . It is cumbersome to do steepest descent transformation for semi-infinite integrals. Thus we want to rewrite them to integrals from $-\infty$ to ∞ by

using the formula of

$$J_\nu(z) = \frac{1}{2} [H_\nu^{(1)}(z) + H_\nu^{(2)}(z)] \quad (65)$$

$$H_\nu^{(2)}(ze^{-\pi j}) = -e^{\nu\pi j} H_\nu^{(1)}(z) \quad (66)$$

The general form of semi-infinite integrals involving J_0 are

$$\begin{aligned} I_0 &= \int_0^\infty \Phi(\lambda^2) \lambda J_0(\lambda) d\lambda \\ &= \frac{1}{2} \int_0^\infty \Phi(\lambda^2) \lambda [H_0^{(1)}(\lambda) + H_0^{(2)}(\lambda)] d\lambda \\ &= \frac{1}{2} \int_0^\infty \Phi(\lambda^2) \lambda [-H_0^{(2)}(-\lambda) + H_0^{(2)}(\lambda)] d\lambda \\ &= \frac{1}{2} \int_{-\infty}^\infty \Phi(\lambda^2) \lambda H_0^{(2)}(\lambda) d\lambda \end{aligned} \quad (67)$$

The general form of semi-infinite integrals involving J_1 are

$$\begin{aligned} I_1 &= \int_0^\infty \Phi(\lambda^2) J_1(\lambda) d\lambda \\ &= \frac{1}{2} \int_0^\infty \Phi(\lambda^2) [H_1^{(1)}(\lambda) + H_1^{(2)}(\lambda)] d\lambda \\ &= \frac{1}{2} \int_0^\infty \Phi(\lambda^2) [H_1^{(2)}(-\lambda) + H_1^{(2)}(\lambda)] d\lambda \\ &= \frac{1}{2} \int_{-\infty}^\infty \Phi(\lambda^2) H_1^{(2)}(\lambda) d\lambda \end{aligned} \quad (68)$$

4.1.6 Total Fields in Cylindrical Coordinate

From the previous two sections, the total fields are written below. It will be seen later that a numerical difficulty is avoided by doing this combination.

$$E_\rho = \pi \sin \phi \int_{-\infty}^{\infty} \left[\omega \mu \tilde{F}_h(\lambda^2, z) + j \tilde{F}'_e(\lambda^2, z) \right] \frac{H_1^{(2)}(k_0 \lambda \rho)}{\rho} d\lambda \\ + \pi \sin \phi \int_{-\infty}^{\infty} -j k_0 \lambda \tilde{F}'_e(\lambda^2, z) H_0^{(2)}(k_0 \lambda \rho) d\lambda \quad (69)$$

$$E_\phi = \pi \cos \phi \int_{-\infty}^{\infty} - \left[\omega \mu \tilde{F}_h(\lambda^2, z) + j \tilde{F}'_e(\lambda^2, z) \right] \frac{H_1^{(2)}(k_0 \lambda \rho)}{\rho} d\lambda \\ + \pi \cos \phi \int_{-\infty}^{\infty} \omega \mu k_0 \lambda \tilde{F}_h(\lambda^2, z) H_0^{(2)}(k_0 \lambda \rho) d\lambda \quad (70)$$

$$E_z = j \pi k_0^2 \sin \phi \int_{-\infty}^{\infty} -\lambda^2 \tilde{F}_e(\lambda^2, z) H_1^{(2)}(k_0 \lambda \rho) d\lambda \quad (71)$$

$$H_\rho = \pi \cos \phi \int_{-\infty}^{\infty} \left[\omega \epsilon \tilde{F}_e(\lambda^2, z) + j \tilde{F}'_h(\lambda^2, z) \right] \frac{H_1^{(2)}(k_0 \lambda \rho)}{\rho} d\lambda \\ + \pi \cos \phi \int_{-\infty}^{\infty} -j k_0 \lambda \tilde{F}'_h(\lambda^2, z) H_0^{(2)}(k_0 \lambda \rho) d\lambda \quad (72)$$

$$H_\phi = \pi \sin \phi \int_{-\infty}^{\infty} \left[\omega \epsilon \tilde{F}_e(\lambda^2, z) + j \tilde{F}'_h(\lambda^2, z) \right] \frac{H_1^{(2)}(k_0 \lambda \rho)}{\rho} d\lambda \\ + \pi \sin \phi \int_{-\infty}^{\infty} -\omega \epsilon k_0 \lambda \tilde{F}_e(\lambda^2, z) H_0^{(2)}(k_0 \lambda \rho) d\lambda \quad (73)$$

$$H_z = j \pi k_0^2 \cos \phi \int_{-\infty}^{\infty} -\lambda^2 \tilde{F}_h(\lambda^2, z) H_1^{(2)}(k_0 \lambda \rho) d\lambda \quad (74)$$

If $\rho = 0$, the total fields are

$$E_\rho = 2\pi \sin \phi \int_0^{\infty} \left[\omega \mu \tilde{F}_h(\lambda^2, z) - j \tilde{F}'_e(\lambda^2, z) \right] \frac{k_0 \lambda}{2} d\lambda \quad (75)$$

$$E_\phi = 2\pi \cos \phi \int_0^{\infty} \left[\omega \mu \tilde{F}_h(\lambda^2, z) - j \tilde{F}'_e(\lambda^2, z) \right] \frac{k_0 \lambda}{2} d\lambda \quad (76)$$

$$E_z = 0 \quad (77)$$

$$H_\rho = 2\pi \cos \phi \int_0^{\infty} \left[\omega \epsilon \tilde{F}_e(\lambda^2, z) - j \tilde{F}'_h(\lambda^2, z) \right] \frac{k_0 \lambda}{2} d\lambda \quad (78)$$

$$H_\phi = 2\pi \sin \phi \int_0^{\infty} - \left[\omega \epsilon \tilde{F}_e(\lambda^2, z) - j \tilde{F}'_h(\lambda^2, z) \right] \frac{k_0 \lambda}{2} d\lambda \quad (79)$$

$$H_z = 0 \quad (80)$$

4.1.7 Solving \tilde{F}_e and \tilde{F}_h

Now let us solve the equation (59) for \tilde{F}_{ei} and \tilde{F}_{hi} ($i = 1, 2$). The air region (region 1) is unbounded, so the general solution of Hertz potential is

$$\tilde{F}_{e1} = Ae^{-\gamma_{z1}(z-d)} \quad (81)$$

$$\tilde{F}_{h1} = De^{-\gamma_{z1}(z-d)} \quad (82)$$

The Hertz potential in the dielectric layer (region 2) is

$$\tilde{F}_{e2} = B \sinh [\gamma_{z2}(d - z)] + C \cosh [\gamma_{z2}(d - z)] \quad (83)$$

$$\tilde{F}_{h2} = E \sinh [\gamma_{z2}(d - z)] + F \cosh [\gamma_{z2}(d - z)] \quad (84)$$

At medium-air interface, applying boundary conditions for TE and TM modes, we get

$$\mu_{r1}\tilde{F}_{h1} = \mu_{r2}\tilde{F}_{h2} \quad (85)$$

$$\frac{\partial \tilde{F}_{h1}}{\partial z} = \frac{\partial \tilde{F}_{h2}}{\partial z} \quad (86)$$

$$\epsilon_{r1}\tilde{F}_{e1} = \epsilon_{r2}\tilde{F}_{e2} \quad (87)$$

$$\frac{\partial \tilde{F}_{e1}}{\partial z} = \frac{\partial \tilde{F}_{e2}}{\partial z} \quad (88)$$

Now we have four equations with six unknowns

$$\epsilon_{r1}A = \epsilon_{r2}C \quad (89)$$

$$\gamma_{z1}A = \gamma_{z2}B \quad (90)$$

$$\mu_{r1}D = \mu_{r2}F \quad (91)$$

$$\gamma_{z1}D = \gamma_{z2}E \quad (92)$$

We need two more equations to solve the problem. They are found by invoking the boundary condition $\hat{z} \times \mathbf{E}_2 = -\mathbf{M}_s$ at $z = 0$ (the tangential component of the electric field has a discontinuity if there is a finite magnetic surface current). But the TE and TM modes are no longer decoupled anymore at $z = 0$ and total electric fields must be used

$$E_{2x}|_{z=0} = E_{2\rho} \cos \phi - E_{2\phi} \sin \phi = 0 \quad (93)$$

$$E_{2y}|_{z=0} = E_{2\rho} \sin \phi + E_{2\phi} \cos \phi = P_m \delta(x) \delta(y) \quad (94)$$

where P_m is the magnetic dipole moment (magnetic current times length).

From (93), we have

$$\omega\mu_2\tilde{F}_{h2} + j\tilde{F}'_{e2} = 0 \Big|_{z=0} \quad (95)$$

The left hand of (94) is

$$E_{2\rho} \sin \phi + E_{2\phi} \cos \phi = 2\pi\omega\mu_2 \int_0^\infty k_0\lambda\tilde{F}_h(\lambda^2, z)J_0(k_0\lambda\rho)d\lambda \quad (96)$$

In the right hand, using the identity in [31], p. 575, we have

$$P_m\delta(x)\delta(y) = \frac{P_m}{2\pi\rho}\delta(\rho) = \frac{P_m}{2\pi} \int_0^\infty \lambda J_0(\lambda\rho)d\lambda = \frac{P_mk_0^2}{2\pi} \int_0^\infty \lambda J_0(k_0\lambda\rho)d\lambda \quad (97)$$

In equating (96) and (97), one get

$$-2j\pi k_0\tilde{F}'_{e2} = 2\pi\omega\mu_2 k_0\tilde{F}_{h2} = \frac{P_mk_0^2}{2\pi} \quad (98)$$

or

$$\tilde{F}_{h2} \Big|_{z=0} = \frac{P_mk_0}{4\pi^2\omega\mu_2} \quad (99)$$

Now we have six equations and six unknowns. Upon solving the equations, we get

$$\begin{aligned} A &= -\frac{jk_0P_m\epsilon_{r2}}{4\pi^2D_{TM}} \\ B &= -\frac{jk_0P_m\epsilon_{r2}\gamma_{z1}}{4\pi^2D_{TM}\gamma_{z2}} \\ C &= -\frac{jk_0P_m\epsilon_{r1}}{4\pi^2D_{TM}} \\ D &= \frac{P_mk_0\gamma_{z2}\mu_{r2}}{4\pi^2\omega\mu_2D_{TE}} \\ E &= \frac{P_mk_0\gamma_{z1}\mu_{r2}}{4\pi^2\omega\mu_2D_{TE}} \\ F &= \frac{P_mk_0\gamma_{z2}\mu_{r1}}{4\pi^2\omega\mu_2D_{TE}} \end{aligned}$$

And for $\tilde{F}_{e,h}$, we have

$$\tilde{F}_{e1} = \frac{-jP_mk_0\epsilon_{r2}}{4\pi^2 D_{TM}} e^{-\gamma_{z1}(z-d)} \quad (100a)$$

$$\tilde{F}_{e2} = \frac{-jP_mk_0}{4\pi^2 D_{TM}\gamma_{z2}} \{ \epsilon_{r2}\gamma_{z1} \sinh[\gamma_{z2}(d-z)] + \epsilon_{r1}\gamma_{z2} \cosh[\gamma_{z2}(d-z)] \} \quad (100b)$$

$$\tilde{F}_{h1} = \frac{P_m\gamma_{z2}}{4\pi^2\eta_0 D_{TE}} e^{-\gamma_{z1}(z-d)} \quad (100c)$$

$$\tilde{F}_{h2} = \frac{P_m}{4\pi^2\eta_0 D_{TE}\mu_{r2}} \{ \mu_{r2}\gamma_{z1} \sinh[\gamma_{z2}(d-z)] + \mu_{r1}\gamma_{z2} \cosh[\gamma_{z2}(d-z)] \} \quad (100d)$$

where

$$D_{TE} = \mu_{r2}\gamma_{z1} \sinh(\gamma_{z2}d) + \mu_{r1}\gamma_{z2} \cosh(\gamma_{z2}d) \quad (101)$$

$$D_{TM} = \epsilon_{r2}\gamma_{z1} \cosh(\gamma_{z2}d) + \epsilon_{r1}\gamma_{z2} \sinh(\gamma_{z2}d) \quad (102)$$

They are the same as the eigen equations we derived earlier.

Their derivatives with respect to z are

$$\tilde{F}'_{e1} = \frac{jP_m\epsilon_{r2}k_0\gamma_{z1}}{4\pi^2 D_{TM}} e^{-\gamma_{z1}(z-d)} \quad (103a)$$

$$\tilde{F}'_{e2} = \frac{jP_mk_0}{4\pi^2 D_{TM}} \{ \epsilon_{r2}\gamma_{z1} \cosh[\gamma_{z2}(d-z)] + \epsilon_{r1}\gamma_{z2} \sinh[\gamma_{z2}(d-z)] \} \quad (103b)$$

$$\tilde{F}'_{h1} = \frac{-P_m\gamma_{z2}\gamma_{z1}}{4\pi^2\eta_0 D_{TE}} e^{-\gamma_{z1}(z-d)} \quad (103c)$$

$$\tilde{F}'_{h2} = \frac{-P_m\gamma_{z2}}{4\pi^2\eta_0 D_{TE}\mu_{r2}} \{ \mu_{r2}\gamma_{z1} \cosh[\gamma_{z2}(d-z)] + \mu_{r1}\gamma_{z2} \sinh[\gamma_{z2}(d-z)] \} \quad (103d)$$

4.2 Sommerfeld Integral Path (SIP)

After the proper integral path has been conceived, it is often deformed to the branch cut (BC) to provide a spectral representation (combination of all possible proper modes including both discrete and continuous modes) or to steepest descent path (SDP) shown in Fig. 17 to approximately the far field efficiently [31]. According to Cauchy theorem,

$$I_{SIP} = I_{NP} - 2\pi j \sum_i \text{Res}[f(k_\rho), k_{\rho i}] \quad (104)$$

where I_{SIP} is the integral along the Sommerfeld integral path (SIP), I_{NP} is the integral along a new path (NP), which is usually chosen to be a BC or a SDP. The last term is the contribution from all poles enclosed by these two paths.

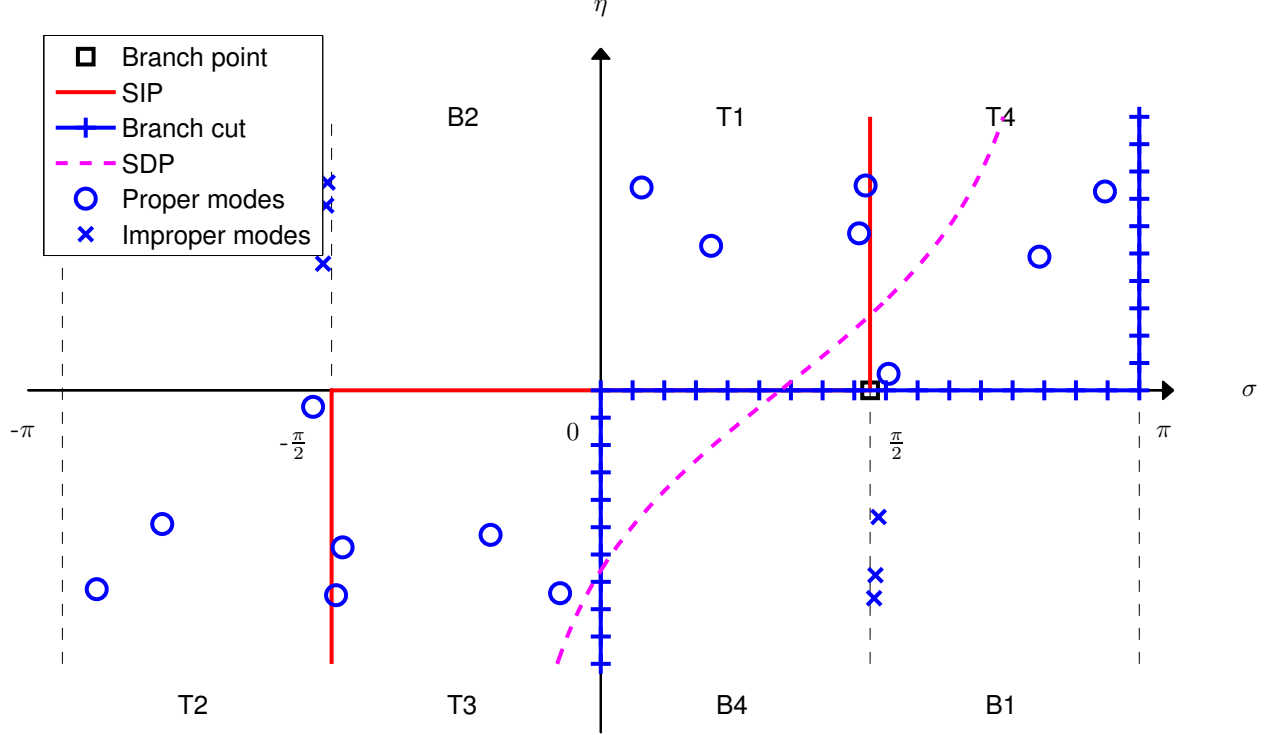


Figure 17: Poles and integral paths in transformed ϕ -plane. Medium parameters are: $\epsilon_{r2} = -2.5 - j0.1$, $\mu_{r2} = -2.5$, $k_0d = 2$. Observation angle $\theta = 60^\circ$ ($z = 0$).

As one of the most commonly used transformations by mathematicians and physicists, the conformal mapping of

$$k_\rho = k_1 \sin \phi \quad (105)$$

where k_1 is the wavenumber in air region and $\phi = \sigma + j\eta$ is a complex number, maps the overlapped Riemann sheet to an unfolded ϕ -plane [36, 41]. Fig. 17 plots poles and integral paths and branch cuts in ϕ -plane in a much clearer way. It is clearly shown that real surface modes, complex surface modes in the third and fourth quadrants, and continuous radiation modes from the branch cuts form a complete mode spectrum of DNG medium.

When the medium is lossy, all poles are not along the real axis in general. So the Sommerfeld integrand can be evaluated along the real axis without any difficulty. But when the medium is lossless, the poles are located on the real axis. All integrands in the last section have D_{TE} or D_{TM} in their denominator. Thus those integrands go to infinite at those poles along the real axis. A common way to address this difficulty is to assume the medium lossy and then monitor how the pole loci change as the loss becomes smaller and smaller. For the lossy medium, the SIP is along the real axis. When the loss is zero, the poles are on real -axis and the SIP should be deformed little away from those poles. From Fig. 14, it is quite natural that one chooses the SIP as shown in Fig. 18(a). As a comparison, Fig. 18(b) shows the SIP for a DPS medium. From Fig. 9, it is observed that the first kind of poles corresponds to forward surface modes (the power flows in the same direction as the phase velocity), while the second kind of poles corresponds to backward surface modes. When the medium is lossy, all first kind poles are located in the second and fourth quadrants and all second kind poles are in the first and third quadrants. Now, consider the cases shown in Fig. 16. The branch C in the figure is the first kind and the branch B is the second kind. Because the power always leaves from the source, one must include the first type of poles with $k_\rho > 0$ and the second type of poles with $k_\rho < 0$ as shown in Fig. 18(a). So both included modes carry away power from the source even they have opposite phase velocity.

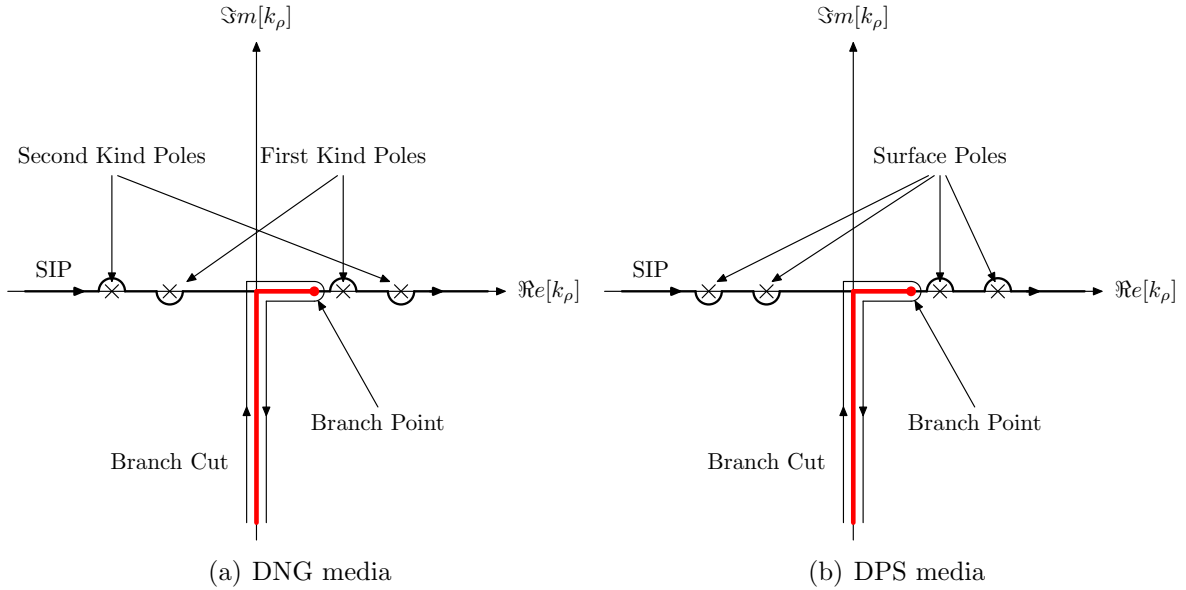


Figure 18: Poles and Sommerfeld integral paths in k_ρ -plane.

4.3 Residue at Origin

Usually, the Sommerfeld integrand involves Bessel/Hankel functions for layered media [31]. As the integral variable approaches the origin, the argument of the Bessel/Hankel function approaches zero. The small argument first order Bessel function can be approximated as [42]

$$J_1(z) \approx \frac{z}{2\Gamma(2)} = \frac{z}{2} \quad (106)$$

$$Y_1(z) \approx -\frac{2}{\pi z} + \frac{2}{\pi} J_1(z) \ln \frac{z}{2} \quad (107)$$

Therefore, the first order Hankel function $H_1^{(2)}(z) = J_1(z) + jY_1(z)$ has a simple pole at origin introduced by its imaginary part $Y_1(z)$. Special care must be taken to account for it otherwise the integral can't be performed. Generally, there are two ways to overcome this difficulty. As an example, we will study a dipole at the interface of a grounded dielectric slab and air.

The first method is to simply combine the TE fields and TM fields together in order to calculate the total field. From [39, 43], the total electrical field at ρ -direction reads

$$E_\rho = \left\{ \int_{-\infty}^{\infty} \left[\omega\mu\tilde{F}_h(\lambda^2, z) + j\tilde{F}'_e(\lambda^2, z) \right] \frac{H_1^{(2)}(k_0\lambda\rho)}{\rho} d\lambda - j \int_{-\infty}^{\infty} \tilde{F}'_e(\lambda^2, z) k_0\lambda H_0^{(2)}(k_0\lambda\rho) d\lambda \right\} \pi \sin \phi \quad (108)$$

where $\lambda = k_\rho/k_0$ and the details of \tilde{F}_e and \tilde{F}_h can be found in 4.1.7.

There is no first order pole in the second term. For the first term, $\omega\mu\tilde{F}_h(\lambda^2, 0) \neq 0$ and $j\tilde{F}'_e(\lambda^2, 0) \neq 0$. However, as proved in [39], their summation $\left[\omega\mu\tilde{F}_h(\lambda^2, z) + j\tilde{F}'_e(\lambda^2, z) \right]$ is zero at origin. Therefore, we have a zero to cancel out the simple pole at origin and the integral will not encounter any problems.

When a combination of the TE and TM fields is not allowed, such as when one wants to calculate the contributions from TE and TM modes separately, we have to resort to the second method: treat TE and TM case separately. Usually, it can be proved to be a Cauchy principal value (CPV) problem and calculated as

$$I = \lim_{\epsilon \rightarrow 0} \left[\int_{-\infty}^{0-\epsilon} + \int_{0+\epsilon}^{\infty} \right] f(z) dz \quad (109)$$

It is more complicated when one deforms the integral path to a BC or a SDP as mentioned previously. In this case, one has to artificially add a small segment to the integral path to close the

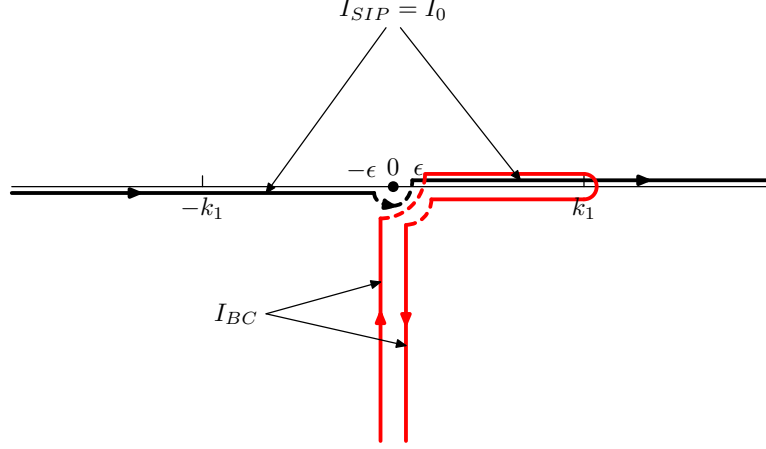


Figure 19: Integral paths near the origin.

integral path since we cannot apply Cauchy's theorem to a CPV integral (because it has a gap), and later subtract it from the result. As an example, let us take a look at the TE component of equation (108)

$$E_\rho = \pi\omega\mu \sin\phi \int_{-\infty}^{\infty} \tilde{F}_h(\lambda^2, z) \frac{H_1^{(2)}(k_0\lambda\rho)}{\rho} d\lambda \quad (110)$$

$$= 2\pi\omega\mu \sin\phi \int_0^{\infty} \tilde{F}_h(\lambda^2, z) \frac{J_1(k_0\lambda\rho)}{\rho} d\lambda \quad (111)$$

Because the Bessel function $J_\nu(z)$ is an entire function, we have

$$I_0 = \int_0^{\infty} f(k_\rho) J_\nu(k_\rho\rho) dk_\rho = \lim_{\epsilon \rightarrow 0} \int_\epsilon^{\infty} f(k_\rho) J_\nu(k_\rho\rho) dk_\rho \quad (112)$$

Now if written in Hankel form, the integral I_0 is

$$I_0 = \lim_{\epsilon \rightarrow 0} \left[\int_{-\infty}^{0-\epsilon} + \int_{0+\epsilon}^{\infty} \right] f(k_\rho) H_\nu^{(2)}(k_\rho\rho) dk_\rho \quad (113)$$

Therefore, the original integral (110) is actually a CPV problem with integral path shown as a solid black line in Fig. 19.

When the integral path is detoured to a BC, in order to apply the Cauchy residue theorem, one has to cover the infinitesimal small gap of the CPV path by deliberately adding a small segment

at origin as drawn with a dashed line in Fig. 19. Now, with that small segment added, one has

$$I_{SIPH} = I_{SIP} + \pi j R^+ \quad (114)$$

where I_{SIP} is the original integral, I_{SIPH} is the integral with the small gap covered, and R^+ is the residue at the positive edge of the branch cut. Similarly for BC path,

$$I_{BCH} = I_{BC} + \frac{\pi j}{2}(R^+ - R^-) \quad (115)$$

where I_{BC} is the CPV integral along BC, I_{BCH} is the integral with the small gap covered, and R^+ and R^- is the residue at the positive and negative edges of the branch cut. Applying the Cauchy residue theorem to I_{SIPH} and I_{BCH} , one has

$$I_{SIPH} = I_{BCH} - 2\pi j \sum_i \text{Res}[f(z), k_i] \quad (116)$$

Finally, one arrives at

$$I_{SIP} = I_{BC} - \frac{\pi j}{2}(R^+ + R^-) - 2\pi j \sum_i \text{Res}[f(z), k_i] \quad (117)$$

The calculation of the residue at the origin is straightforward. When $\lambda \rightarrow 0$, the integrand is approximated as

$$\begin{aligned} \tilde{F}_h(\lambda^2, z) \frac{H_1^{(2)}(k_0 \lambda \rho)}{\rho} &= \frac{\tilde{F}_h(0, z)}{\rho} [J_1(k_0 \lambda \rho) - j Y_1(k_0 \lambda \rho)] \\ &\approx \frac{\tilde{F}_h(0, z)}{\rho} \frac{2j}{\pi k_0 \lambda \rho} \end{aligned} \quad (118)$$

The residue of the integrand at the origin is then

$$R^\pm = \frac{2j \tilde{F}_h(0, z)}{\pi k_0 \rho^2} \Big|_{\gamma_{z1} = \pm j k_1} \quad (119)$$

Fortunately, it is only in rare cases that one needs to pay attention to the aforementioned details. Most of the numerical calculations can be performed using the Bessel function form of the Sommerfeld integrals. Therefore, the original $[-\infty, \infty]$ integral range is folded to $[0, \infty]$, and there is no problem at the origin. One must pay attention to including the pole at the origin only when the complex plane analysis is needed.

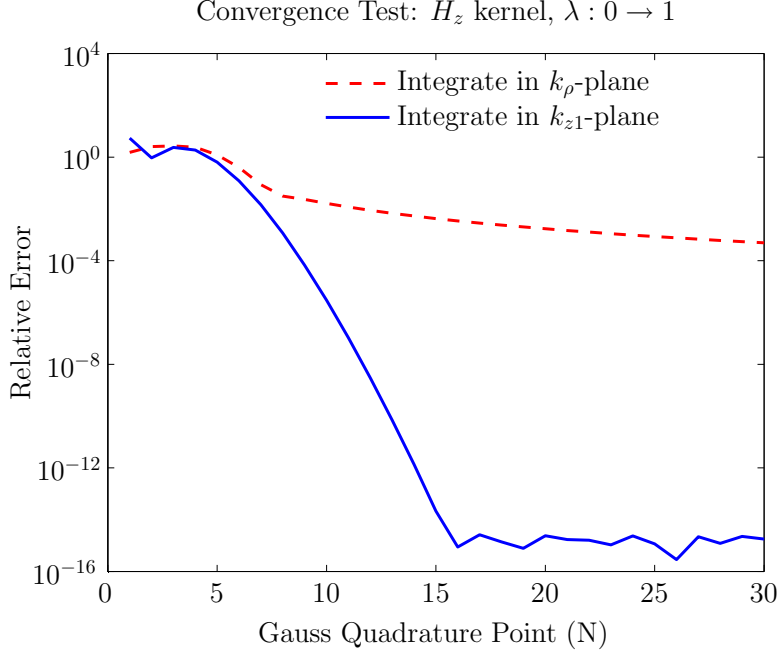


Figure 20: Convergence tests of equation (120) and (123).

4.4 Numerical Integration Along SIP

It is found that the convergence of the Sommerfeld integral along SIP in k_ρ -plane is very slow. As an example, we test two integrals that have exact solutions. They are H_z and E_z in free space

$$H_z = \int_0^\infty \lambda^2 e^{-\gamma_{z1}z} J_1(k_0\lambda\rho) d\lambda \quad (120)$$

$$E_z = \int_0^\infty \lambda^2 \frac{1}{\gamma_{z1}} e^{-\gamma_{z1}z} J_1(k_0\lambda\rho) d\lambda \quad (121)$$

For simplicity purpose, both H_z and E_z in above equations are normalized with the coefficient:

$$\frac{-2j\pi k_0^2 P_m \cos \phi}{4\pi^2 \eta_0 \mu_{r1}} \quad (122)$$

In (120), the integrand is smooth along the integral path. However, its first derivative has singularity at $\lambda = 1$. For this reason, the convergence is very slow. The integrand of (121) is even worse as its integrand blows up at $\lambda = 1$. But it is still integrable at $\lambda = 1$.

The above two equations are transformed to λ_{z1} -plane, and now $\lambda_{z1} = k_{z1}/k_0$ becomes the integration dummy variable. Also changed is the integral path that is mapped to a different shape in λ_{z1} -plane

$$H_z = \left[\int_1^0 + \int_0^{-j\infty} \right] \lambda \lambda_{z1} e^{-\gamma_{z1} z} J_1(k_0 \lambda \rho) d\lambda_{z1} \quad (123)$$

$$E_z = \left[\int_1^0 + \int_0^{-j\infty} \right] \lambda e^{-\gamma_{z1} z} J_1(k_0 \lambda \rho) d\lambda_{z1} \quad (124)$$

The comparisons of convergences of (120) and (123) are plotted in Fig. 20. The integration in k_{z1} -plane (or λ_{z1} -plane) is far superior to the integration in k_ρ -plane (or λ -plane). Similar conclusions apply to (121) and (124). The reason is because (123) and (124) now have continuous high order derivatives and thus their convergence is much faster than (120) and (121).

5 Numerical Examples and Optimization for Directivity

In this section, two important radiation problems — a horizontal magnetic dipole (HMD) on PEC covered with DNG media and a horizontal electric dipole (HED) at the interface of grounded DNG media and air shown in Fig. 16 — are solved using Sommerfeld integrations. They are of great importance in that they provide Green's function to slot antennas and microstrip patch antennas, because Green's functions are electric and magnetic fields generated by electric dipoles on the interface or magnetic dipoles on the metal surface. We also investigated the radiation intensity and directivity of electric/magnetic dipoles over a grounded slab to find optimal values of the material parameters and thickness for a given frequency.

5.1 Numerical Example of New SIP Path for DNG Media

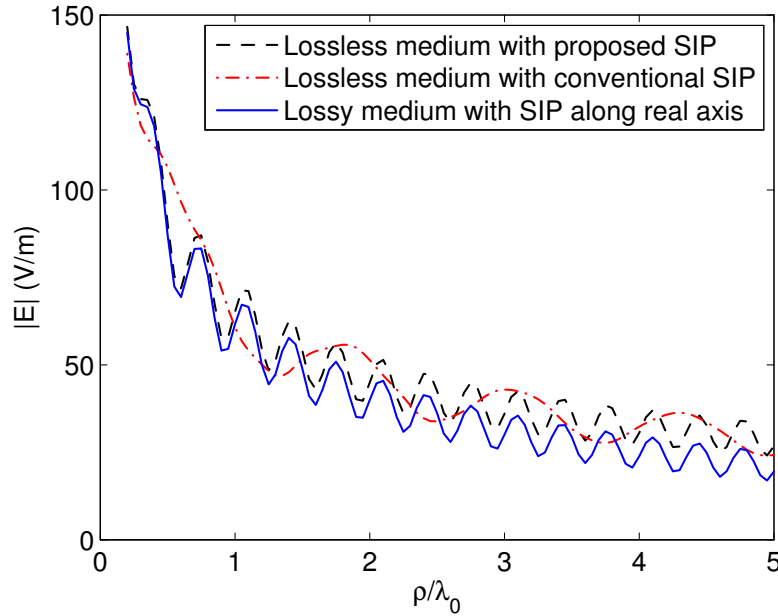


Figure 21: The examination of the proper Sommerfeld integral path for DNG medium. $k_0 d = 2$, $\epsilon_{r2} = -2.5 - j\delta$, $\mu_{r2} = -2.5$. Solid line is for $\delta = 0.01$; dashed line is for $\delta = 0$ and our proposed SIP; dash dot line is for $\delta = 0$ and conventional SIP.

The first numerical example is to verify the validation of the newly proposed Sommerfeld integral path for DNG media. The electric fields of a horizontal electric dipole at the interface of air and a grounded dielectric DNG medium slab are calculated along the interface by our program which can handle both lossy and lossless media. In Fig. 21, the solid line is for a lossy medium whose

permittivity is $\epsilon_{r2} = -2.5 - 0.01j$. As the loss keeps all surface mode poles off the real axis, *i.e.*, k_ρ -axis, we do not encounter any numerical troubles. More importantly, the SIP can be unambiguously defined along the real axis and both ordinary surface wave modes with the first kind of pole (such as TM_2) and with both kind of pole (such as TE_3) are excited, which can be confirmed by Fig. 7 with $k_0d = 2$. The dashed line in Fig. 21 shows the total field (as a function of distance from source) for the same medium with loss removed, using the new SIP proposed in Section 4. It is seen that these two lines are closely lined up at the near field where the attenuation is hardly appreciable. As we move away to the far field, the electric field in the lossy medium undergoes more attenuation and we see more deviations from the dashed line, but they exhibit the same oscillation behavior with the same rhythms. This proves the correctness of the new SIP. The dash-dot line is the calculation for the same lossless medium, except that the SIP for DPS medium is used, as shown in Fig. 18(b). It deviates from either the blue solid line or dashed line. In summary, Fig. 21 justifies our proposed Sommerfeld integral path.

5.2 The Discrete Pole Contribution of DNG Media

The second example solves a horizontal magnetic dipole on a PEC covered by a DNG slab as shown in Fig. 16(a). The problem is also studied by P. Baccarelli *et al.* [18]. The permittivity and permeability of this material are modeled as [6, 2]

$$\mu_r(\omega) = 1 - \frac{F\omega^2}{\omega^2 - \omega_0^2} \quad \text{and} \quad \epsilon_r(\omega) = 1 - \frac{\omega_p^2}{\omega^2} \quad (125)$$

where $F = 0.56$, $\omega_0/2\pi = 4$ GHz, and $\omega_p/2\pi = 10$ GHz. The material simultaneously exhibits negative permittivity and permeability from $f = 4$ GHz to 6.03 GHz [18].

Figure 22 plots the total electric field as a blue solid line and it exactly agrees with [18]. Also plotted in red dashed line is the electric field from the discrete mode contribution. This includes the evanescent surface mode TM_0 (first kind), complex surface modes TM_2 and TE_3 , and all other higher order complex modes. A very interesting phenomenon is observed: unlike a DPS medium, which always has at least one surface pole whose contribution goes to infinity as the observation point moves towards the source, the DNG medium's large number of discrete poles tends to have some cancellation effect that limits their contribution to a finite value even when the observation point is very close to the source. Notice that in our calculation, 400 modes are used in order to achieve accurate pole contributions. For the field of single mode, it should be inverse proportional to the square root of ρ . But our numerical results from the figure show that the total pole contributions (with 400 poles) become finite when the ρ approaches zero (the red dashed line). The similar plot is also given in [18] with smaller number of modes included.

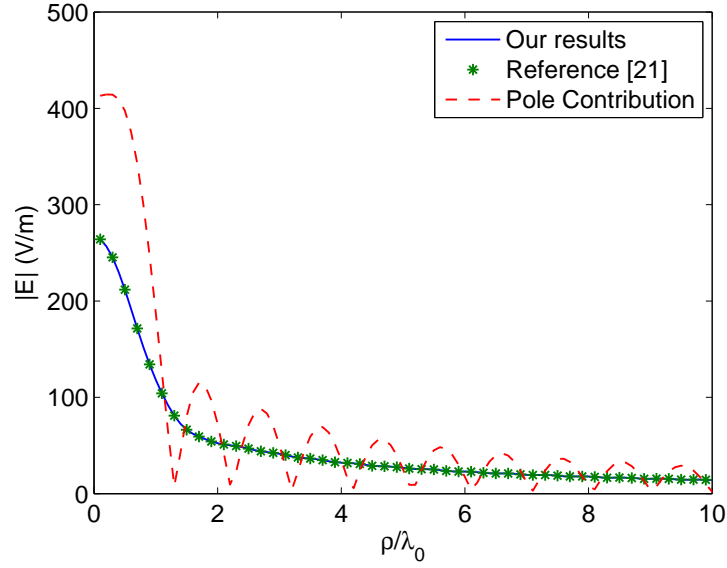


Figure 22: The comparison of our results to reference [18]. The medium parameters are exactly the same as in [18], the thickness is 60 mm, and the frequency is 5.6 GHz.

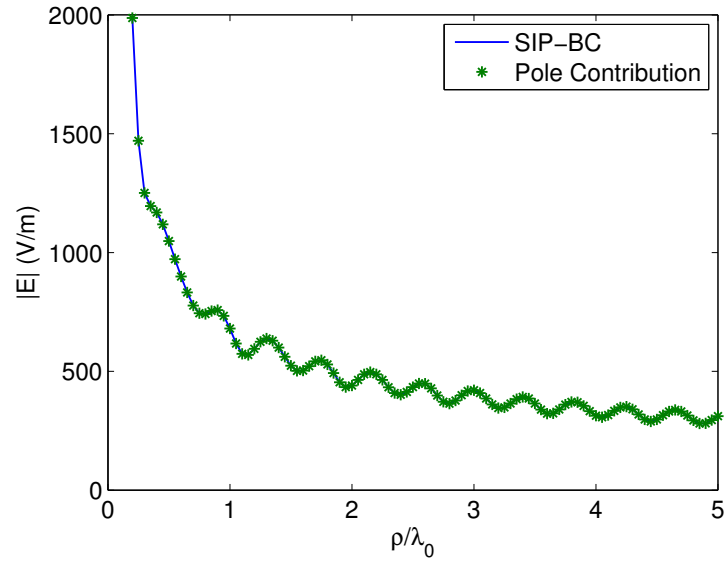


Figure 23: The electric fields due to the pole contributions and the difference between the integrals along the SIP and BC. The medium parameters are given by (125), the frequency is 4.8 GHz, and the thickness is 20 mm.

In Figure 23, we plot the electric fields due to the pole contributions and difference between the integrals along the proposed SIP and along the BC. The frequency is 4.8 GHz and the thickness of the slab is 20 mm. At this electric size, the evanescent surface mode TE_1 (second kind) and ordinary surface mode TM_2 (both kinds), and complex surface modes are excited [21]. Excellent agreement is observed from Fig. 23 and the relation shown in (104) is satisfied, which verifies the correctness of our new proposed Sommerfeld integral path for DNG medium.

5.3 3-D Radiation Patterns (linear scale) of HED and HMD with DNG Media

The radiation patterns associated with the structures in Fig. 16 are shown in Fig. 24. The media parameter defined in (125) is used in the calculations. The frequency is chosen at $f = 5.943$ GHz as it gives the best directivity [18, 39]. The medium parameters at this frequency are $\epsilon_{r2} = -1.831$ and $\mu_{r2} = -0.0238$. The thickness of the dielectric slab is $d = 60$ mm ($k_0d = 7.47$ and $kd = 1.56$). Maximum directivities are observed at the z -direction (broadside): 26.8 dB for HMD and a smaller number 17.2 dB for HED due to some cancellation of the image from the ground. They are drastically larger than the values of 8.5 dB and 12.0 dB, respectively, obtained for a conventional DPS slab with ($\epsilon_r = 2.55$ and $\mu_r = 1$ at $f = 5.4$ GHz). Unlike the electromagnetic fields in conventional DPS media where some of the energy is carried away by surface wave, the fields in DNG medium tend to decay more slowly due to the existence of complex modes. Therefore, the dipole with DNG media has a much larger equivalent aperture size that results in a much narrower radiation beam. The microstrip antennas with DNG media can have compact size comparing the antennas with conventional DPS media.

5.4 Optimization for Directivity

One of the research interests is to find optimized values for the constitutive parameters of the structure shown in Fig. 16, for a specified k_0d so that we can obtain high directivity in the broadside direction. The HMD case (Fig. 16(a)) is taken as an example in the following discussion. In reference [18], it was found that that highly directive beams can be obtained by employing substrates with a large ratio of $|\epsilon_r|/|\mu_r|$, because the broadside power density $P(\theta = 0)$ is proportional to this ratio.

We further optimize k_0d , ϵ_r , and μ_r to get the maximum directivity. Figure 25 shows how the broadside directivity changes along ϵ_r and μ_r for a given k_0d :

Figure 25 gives us an idea that for a given k_0d , the broadside directivity may reaches a maximum when the product of ϵ_r and μ_r is equal to a certain value. This idea is confirmed by a further

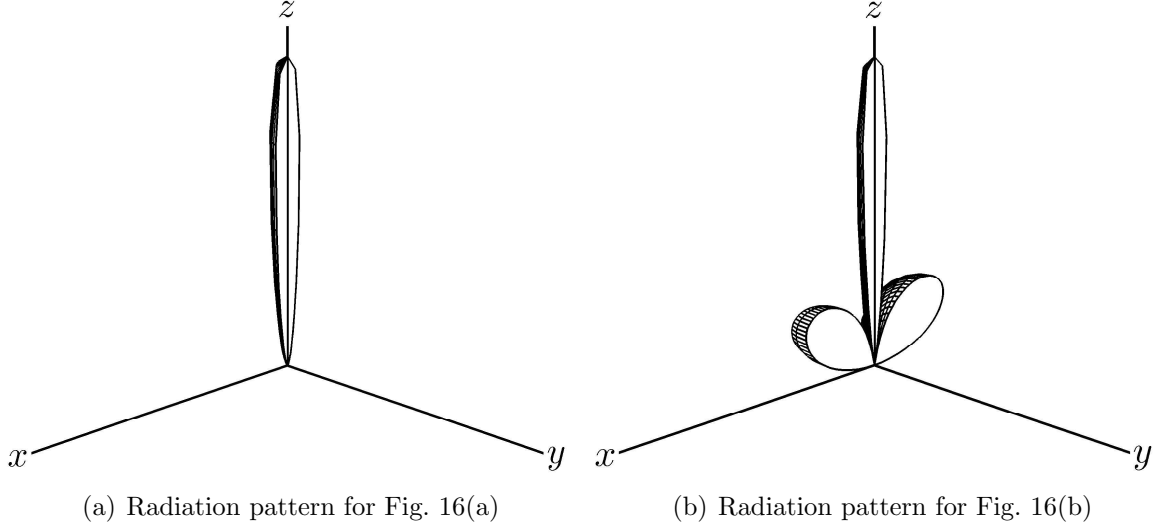


Figure 24: Radiation patterns of HMD and HED associated with DNG media at $f = 5.943$ GHz.

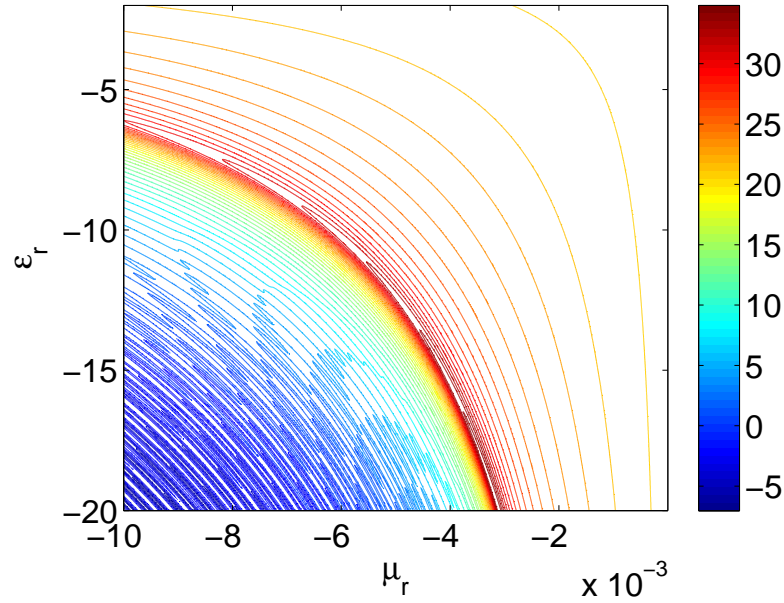


Figure 25: Contour plot of the directivity at the broad side over different ϵ_r and μ_r , $d/\lambda_0 = 1$.

investigation of the data constructing Fig. 25. From that data we can also get the value of $\epsilon_r \mu_r$ for

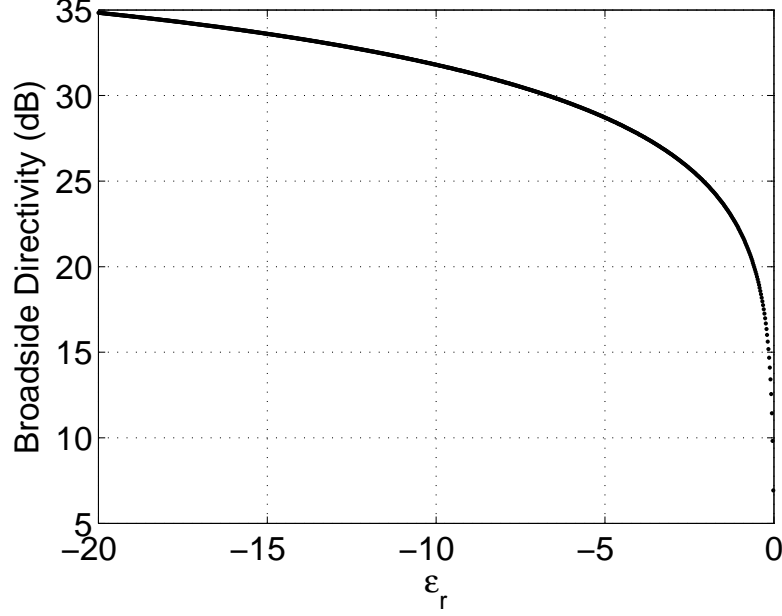


Figure 26: Broadside directivity as a function of ϵ_r ($\epsilon_r \mu_r = 0.062$, $d/\lambda_0 = 1$).

$d/\lambda_0 = 1$ ($k_0 d = 2\pi$) is about 0.062. Numerical results of cases with different $k_0 d$ values lead to the same conclusion: for a given $k_0 d$, the broadside directivity is only a function of ϵ_r . Figure 26 is presented as a validation of this conclusion. Figure 26 also shows that a larger $|\epsilon_r|$ gives a larger broadside directivity. Because the product of ϵ_r and μ_r is kept constant, the larger ϵ_r is, the larger is the ratio of $|\epsilon_r|/|\mu_r|$. This agrees with the finding in [18].

To verify that $\epsilon_r \mu_r$ is unique to have maximum directivity for a given d/λ_0 , we examine for a small range of $\epsilon_r \mu_r$. Figure 27 is the contour plot of maximum broadside directivity as a function of ϵ_r and the product of $\epsilon_r \mu_r$. From this figure we can see that for any ϵ_r , the maximum directivity is always obtained when $\epsilon_r \mu_r$ is the same certain value (some value between 0.06 and 0.065). So we can conclude that to have maximum broadside directivity for a given d/λ_0 , the product of $\epsilon_r \mu_r$ should be a unique value $c(k_0 d) = \epsilon_r \mu_r$. Hereby we investigate the dependence between $c(k_0 d)$ and electric size. For the electric size in the range of our interest, that is 0.1 to 1 wavelength, we find the optimized $c(k_0 d)$ at 10 different electric sizes between 0.1 and 1 wavelength and fit the data with a simple curve. The fitting result is presented in Fig. 28 and the fitted formula is given as

$$c(k_0 d) = \frac{2.4635}{(k_0 d)^2} = \frac{0.0624}{(d/\lambda_0)^2} \quad (126)$$

where $c(k_0d) = \epsilon_r \mu_r$.

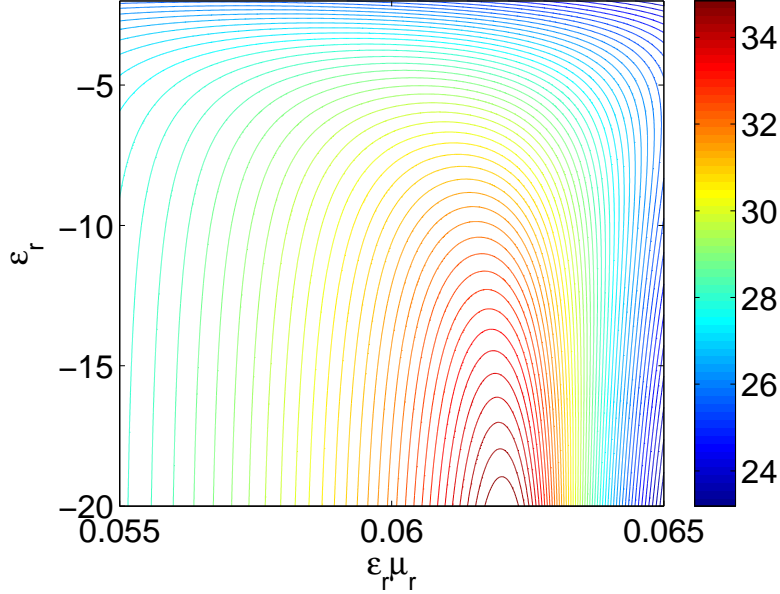


Figure 27: Contour plot of the directivity at the broad side over different ϵ_r and $\epsilon_r \mu_r$, $d/\lambda_0 = 1$.

Now for any given electric size (d/λ_0 or k_0d) and relative permittivity ϵ_r we can calculate the optimized relative permeability μ_r , so that we can get the maximum broadside directivity.

From the discussion above, we can summarize a procedure to get optimized constitutive parameters for a given k_0d :

1. For any given d/λ_0 (or k_0d), we set ϵ_r to a proper value. Any ϵ_r in the range specified by the application will do; it's not important in this step because we just want to find the product of ϵ_r and μ_r here, which is ϵ_r independent. And then we do a one variable optimization to find the product of ϵ_r and μ_r so that the maximum broadside directivity is obtained. In Matlab, there are certain commands which can help with the optimization.
2. If there is a range limit for ϵ_r , the directivity at the broad side is always obtained at the largest absolute value of ϵ_r . The corresponding value of μ_r is obtained by using $\mu_r = c(k_0d)/\epsilon_r$.

From the discussion above, we know that the maximum broadside directivity can be expressed as a function of electric size d/λ_0 and relative permittivity ϵ_r . Now we provide an approximate

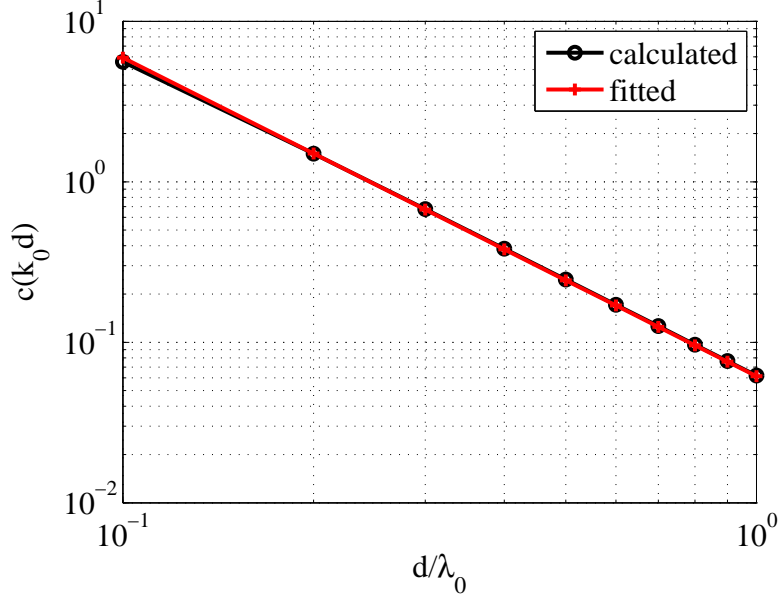


Figure 28: $c(k_0 d)$ as a function of electric size.

formula to estimate the maximum broadside directivity of this structure. To get the formula, the maximum broadside directivities for different d/λ_0 and ϵ_r are calculated numerically. We use a formula with simple form and un-determined coefficients to fit the data and get the coefficients. Finally we find that the maximum broadside directivity D_0 can be obtained using the approximate formula:

$$D_0 = 155 \left(\frac{d}{\lambda_0} \right)^{8/3} |\epsilon_r| \quad (127)$$

Figure 29 shows the validation of our approximate formula. By using Equation (127), we can obtain an estimated maximum broadside directivity for a given electric size and relative permittivity. This formula is derived under the condition that $|\epsilon_r| \gg |\mu_r|$ and for a given ϵ_r and μ_r that satisfy Equation (126). The numerical results in Fig. 29 show that this formula works in the range $0.2 < d/\lambda_0 < 1$.

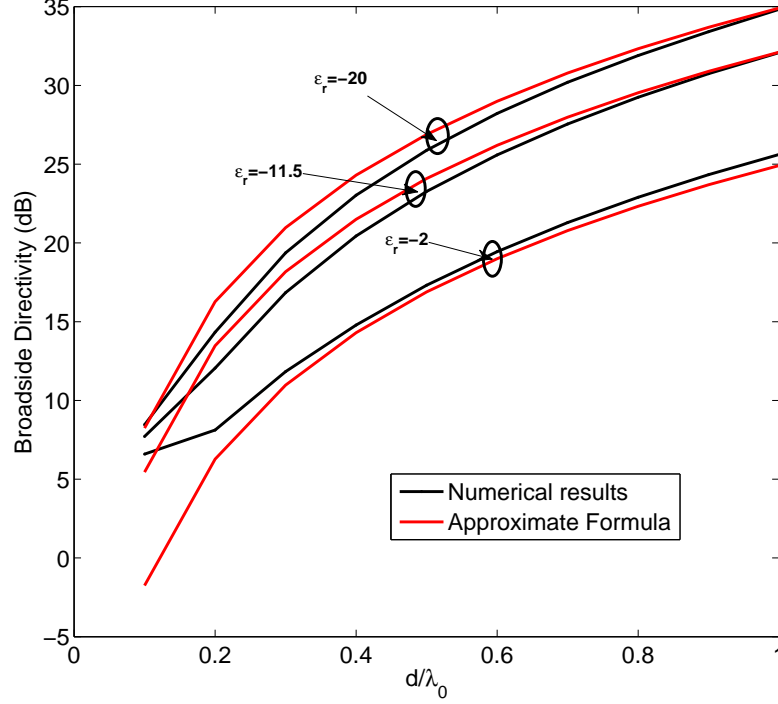


Figure 29: Approximate formula (Equation (127)) vs numerical results.

6 Conclusions, Publications, and Significant Events

In this final report, we first review the mode properties of a grounded DNG medium slab. The complexity of the mode spectrum and pole behavior under parameter and frequency variations demands a new Sommerfeld integral path that is different from the SIP for a conventional DPS medium, as shown in Fig. 18(b). Two numerical issues associated with Sommerfeld integrals are studied in great detail. A new Sommerfeld integral path is suggested to increase numerical convergence by eliminating singularities of the integrand or the derivatives of the integrand. Numerical examples are given to validate the necessity of a new Sommerfeld integral path. The electromagnetic fields and radiation patterns of horizontal electric and magnetic dipoles with slabs of DNG media are plotted. Due to the slowly decaying fields along the interface, the radiation directivity is greatly enhanced.

We investigated the radiation intensity and directivity of electric/magnetic dipoles over a grounded slab to find optimal values of material parameters and thickness for a given frequency. We optimize the directivity over the thickness and the constitutive parameters. It is found that for

a slab with a fixed electric size (proportional to the product of the thickness and frequency), the directivity reaches the maximum when the product of ϵ_r and μ_r is constant, which depends on the electric size only. The maximum directivity is proportional to the ratio between ϵ_r and μ_r . Finally, the optimized structure to get maximum directivity at broadside is investigated and fitted formula for the maximum directivity is provided.

In summary, we have

1. Found complete spectrum in ground DNG slab, studied surface wave suppression.
2. Derived the power flow for all discrete surface wave modes and found that the complex wave modes in lossless slab do not carry away any power.
3. Plotted loci of complex (leaky) wave modes as functions of thickness and loss.
4. Derived field expressions for a HMD and HED over a grounded DNG slab and found that the radiation patterns have large directivity.
5. Developed empirical formula for the directivity at broadside.
6. Found the correct Sommerfeld integral path for a DNG slab.

Publications

W.W. Shu and J.M. Song, "Sommerfeld Integral Path for Layered Double Negative Metamaterials," IEEE Transactions on Antennas and Propagation, under review.

Collaborations

We have collaborated with Dr. Shore (AFRL Hanscom) and Dr. Yaghjian (self-employed) on leaky wave properties on dielectric slab and hybridization of analytical and numerical approaches to study the band structures of metamaterials.

Significant Events

1. The PI attended the progress review meeting on April 27-28, 2010 in Arlington, Virginia, and briefed the audience on our latest progress on this project.
2. On July 7, 2010, the PI visited AFRL-Hanscom and discussed with Drs. Shore and Yaghjian on our recent progress and future directions for this project.
3. The PI attended 2011 Electromagnetics Contractors Meeting organized by Dr. Arje Nachman from AFOSR between January 4 and 5 and met Dr. Yaghjian and other researchers in this area.

What is Next?

1. Design antennas using DNG metamaterials: design patch antennas, aperture antennas with excitation of leaky waves, optimize microstrip antenna performance (gain and bandwidth) for different dimensions, thickness, loss, permittivity, and permeability.
2. Design antennas with real structures: use periodic structures for substrate and superstrate. and work with experimental experts to make such antennas.
3. Reduce loss in metamaterials and increase antenna efficiency.

These antennas may have significant impacts on applications for Air Force.

References

- [1] R. W. Ziolkowski and N. Engheta, “Special issue on metamaterials,” vol. 51, pp. 2546–2750, October 2003.
- [2] J. B. Pendry, A. J. Holden, D. J. Robbins, and W. J. Stewart, “Magnetism from conductors and enhanced nonlinear phenomena,” vol. 47, pp. 2075–2084, November 1999.
- [3] D. R. Smith, W. J. Padilla, D. C. Vier, S. C. Nemat-Nasser, and S. Schultz, “Composite medium with simultaneously negative permeability and permittivity,” *Phys. Rev. Lett.*, vol. 84, pp. 4184–4187, May 2000.
- [4] S. C. N.-N. R. A. Shelby, D. R. Smith and S. Schultz, “Microwave transmission through a two-dimensional, isotropic, left-handed metamaterial.”
- [5] V. G. Veselago, “The electrodynamics of substances with simultaneously negative values of ϵ and μ ,” *Soviet Physics USPEKI*, vol. 10, pp. 509–514, 1968.
- [6] J. B. Pendry, A. J. Holden, W. J. Stewart, and I. Youngs, “Extremely low frequency plasmons in metallic mesostructures,” *Phys. Rev. Lett.*, vol. 76, pp. 4773–4776, June 1996.
- [7] J. B. Pendry, “Negative refraction makes a perfect lens,” *Phys. Rev. Lett.*, vol. 85, pp. 3966–3969, October 2000.
- [8] R. A. Shelby, D. R. Smith, and S. Schultz, “Experimental verification of a negative index of refraction,” *Science*, vol. 292, pp. 72–79, April 2001.
- [9] D. R. Smith and N. Kroll, “Negative refractive index in left-handed materials,” *Phys. Rev. Lett.*, vol. 85, pp. 2933–2936, October 2000.
- [10] P. M. s and C. M. Soukoulis, “Numerical studies of left-handed materials and arrays of split ring resonators,” *Phys. Rev. E*, vol. 65, p. 036622, 2002.
- [11] A. Alù and N. Engheta, “Pairing an epsilon-negative slab with a mu-negative slab: resonance, tunneling and transparency,” vol. 51, pp. 2558–2571, October 2003.
- [12] C. Caloz and T. Itoh, “Transmission line approach of left-handed (LH) materials and microstrip implementation of an artificial LH transmission line,” vol. 52, pp. 1159–1166, May 2004.
- [13] I.-H. Lin, M. DeVincentis, C. Caloz, and T. Itoh, “Arbitrary dual-band components using composite right/left-handed transmission lines,” vol. 52, pp. 1142–1149, April 2004.

- [14] R. Mittra, K. Rajab, and M. T. Lanagan, "Size reduction of microstrip antennas using metamaterials," in *IEEE Antennas Propag. Soc. Int. Symp.*, Washington, DC, 2005, pp. 296–299.
- [15] A. Erentok and R. W. Ziolkowski, "Development of epsilon-negative (ENG) metamaterials for efficient electrically small antenna applications," in *IEEE Antennas Propag. Soc. Int. Symp.*, Washington, D. C., 2005, pp. 304–307.
- [16] R. Ziolkowski and A. D. Kipple, "Application of double negative materials to increase the power radiated by electrically small antennas."
- [17] B.-I. Wu, T. M. Grzegorzczuk, Y. Zhang, and J. A. Kong, "Guided modes with imaginary transverse wave number in a slab waveguide with negative permittivity and permeability," *J. Appl. Phys.*, vol. 93, pp. 9386–9388, 2003.
- [18] P. Baccarelli, P. Burghignoli, F. Frezza, A. Galli, P. Lampariello, G. Lovat, and S. Paulotto, "Effects of leaky-wave propagation in metamaterial grounded slabs excited by a dipole source," vol. 53, pp. 32–44, January 2005.
- [19] J. L. X. D. C. J. P. T. Grzegorzczuk, C. D. Moss and J. A. Kong, "A study of using metamaterials as antenna substrate to enhance gain."
- [20] M. L. S. N. Burokur and S. Toutain, "Theoretical investigation of a circular patch antenna in the presence of a left-handed medium."
- [21] P. Baccarelli, P. Burghignoli, F. Frezza, A. Galli, P. Lampariello, G. Lovat, and S. Paulotto, "Fundamental modal properties of surface waves on metamaterial grounded slabs," vol. 53, pp. 1431–1442, April 2005.
- [22] W. W. Shu and J. M. Song, "Wave propagation in grounded dielectric slabs with double negative metamaterials."
- [23] H. Cory and A. Barger, "Surface-wave propagation along a metamaterial slab," *Microwave Opt. Technol. Lett.*, vol. 38, pp. 392–395, 2003.
- [24] H. Dong and T. X. Wu, "Analysis of discontinuities in double-negative (DNG) slab waveguides," *Microwave Opt. Technol. Lett.*, vol. 39, pp. 483–488, October 2003.
- [25] I. S. Nefedov and S. A. Tretyakov, "Waveguide containing a backward-wave slab," *Radio Sci.*, vol. 38, pp. 1101–1109, November 2003.

- [26] I. W. Shadrivov, A. A. Sukhorukov, and Y. S. Kivshar, “Guided modes in negative-refractive-index waveguides,” *Phys. Rev. E, Stat. Phys. Plasmas Fluids Relat. Interdiscip. Top.*, vol. 67, pp. 057 602–057 602, 2003.
- [27] W. Shu and J. M. Song, “Complete mode spectrum of a grounded dielectric slab with double negative metamaterials,” *Progress In Electromagnetics Research*, vol. 65, pp. 103–123, 2006.
- [28] C. Li, Q. Sui, and F. Li, *Progress In Electromagnetics Research*. Cambridge, MA: EMW Publishing, 2005, vol. 51, ch. Complex guided wave solutions of grounded dielectric slab made of metamaterials, pp. 187–195.
- [29] P. Baccarelli, P. Burghignoli, G. Lovat, and S. Paulotto, “Surface-wave suppression in a double-negative metamaterial grounded slab,” vol. 2, pp. 269–272, 2003.
- [30] W. Shu, J. M. Song, and L. Zhang, “Novel properties of double negative metamaterials in dielectric slabs and microstrip lines,” in *URSI Radio Science Meeting*, Washington, DC, June 2005.
- [31] W. C. Chew, *Waves and Fields in Inhomogeneous Media*. Piscataway, New Jersey: IEEE Press, 1995.
- [32] W. Chew, “Sommerfeld integrals for left-handed materials,” *Microwave and Optical Technology Letters*, vol. 42, no. 5, pp. 369–373, September 2004.
- [33] L. Landau, E. Lifshitz, and L. Pitaevskii, *Electrodynamics of Continuous Media*, 2nd ed. Oxford, England: Butterworth-Heinenann, 1984.
- [34] G. W. Hanson and A. B. Yakovlev, *Operator Theory for Electromagnetics*, New York: Springer-Verlag, 2001.
- [35] C. A. Balanis, *Advanced Engineering Electromagnetics*. John Wiley Sons, Inc., 1989.
- [36] R. E. Collin, *Field Theory of Guided Waves*, 2nd ed. Piscataway, New Jersey: IEEE Press, 1991.
- [37] A. Alù and N. Engheta, *An overview of salient properties of planar guidedwave structures with double-negative (DNG) and single-negative (SNG) layers*, Chapter 9 in *Negative-Refractive Metamaterials: Fundamental Principles and Applications*, edited by G. V. Eleftheriades and K. G. Balmain, New Jersey: John Wiley & Sons, pp. 339–380, 2005.
- [38] A. A. Oliner, “Leakage from higher modes on microstrip line with applications to antennas,” *Radio Sci.*, vol. 22, pp. 907–912, 1987.

- [39] W. Shu, “Electromagnetic waves in double negative metamaterials and study on numerical resonances in the method of moments (mom),” Ph.D. dissertation, Iowa State University, 2008.
- [40] T. Tamir and F. Y. Kou, “Varieties of leaky waves and their excitation along multilayered structures,” *IEEE J. Quantum Electronics*, vol. 22, no. 4, pp. 544-551, April 1986.
- [41] J. A. Kong, *Electromagnetic Wave Theory*, 2nd ed. New York: Wiley, 1990.
- [42] M. Abramowitz and I. A. Stegun, Eds., *Handbook of Mathematical Functions*. New York: Dover Publications, 1970.
- [43] A. Benalla and K. C. Gupta, “Multiport network model for rectangular microstrip patches covered with a dielectric layer,” *IEEE J. Quantum Electronics*, vol. 22, no. 4, pp. 377-383, April 1986.